The Effect of Drifter GPS Errors on Estimates of Submesoscale Vorticity

MATTHEW S. SPYDELL AND FALK FEDDERSEN

Scripps Institution of Oceanography, University of California, San Diego, La Jolla, California

JAMIE MACMAHAN

Naval Post Graduate School, Monterey, California

(Manuscript received 25 June 2019, in final form 22 August 2019)

ABSTRACT

Differential kinematic flow properties (DKP), such as vertical vorticity, have been estimated from surface drifters. However, previous DKP error estimates were a posteriori and did not include correlated errors across drifters. To accurately estimate submesoscale ($\leq$1 km) DKPs from drifters, errors must be better understood. Here, the a priori vorticity standard error is derived that depends upon the number of drifters in the cluster, the drifter cluster major and minor axes lengths, the instrument velocity error, and the cross-drifter error correlation. Two stationary GPS experiments, with zero vorticity, were performed at separations of $O(10^1–10^3)$ m to understand vorticity error and test the derivation using 1 Hz position differences and Doppler shift velocities. Vorticity errors of $\pm 5f$ (where f is the local Coriolis parameter) were found for $\approx$40 m separations. The frequency-dependent velocity variances and GPS-to-GPS correlations are quantified. Vorticity estimated with a ''blended'' velocity has reduced error. The stationary vorticity error can be well predicted given velocity error, correlation, and minor axis length. Vorticity error analysis is applied to submesoscale-sampling in situ GPS drifters near Point Sal, California. The derivation predicts when large high-frequency vorticity fluctuations (indicating noise) occur. Previously, cluster area or ellipticity were used as criteria to distinguish error. We show that the drifter cluster minor axis (narrowness) is a key time-dependent factor affecting vorticity error, and even for velocity errors $<0.004\ \mathrm{m\ s^{-1}}$, the vorticity error exceeds $\pm 5f$ when cluster minor axis $<$50 m. These results will aid submesoscale drifter deployment planning.

1. Introduction

Lagrangian drifters play an important role in understanding ocean currents and eddies from large open-ocean scales (hundreds of kilometers; e.g., Lumpkin and Johnson 2013) to small surfzone scales (5 m; e.g., Spydell et al. 2007; Brown et al. 2009). Drifter observations are used to study surface (Lumpkin and Johnson 2013) and subsurface (Ollitrault and Colin de Verdière 2014) currents, estimate absolute and relative diffusivity and Lagrangian time scales, and infer scale-selective diffusivities [for a review, see LaCasce (2008)]. Drifters are tracked with various methods, a brief history of which is found in Lumpkin et al. (2017). Many modern drifters are tracked with GPS due to its affordability and accuracy (e.g., Schmidt et al. 2003; Ohlmann et al. 2017; Novelli et al. 2017).

In addition to mean circulation patterns and diffusivities, surface horizontal divergence ($dU/dx + dV/dy$) and vertical vorticity ($dV/dx - dU/dy$) have been estimated from drifters. These, and other fluid differential kinematic properties (DKP), are found from the positions and velocities of three or more drifters from which all horizontal velocity gradients (dU/dx, dU/dy, dV/dx, and dV/dy) can be estimated using a least squares (LS) technique, first described in Molinari and Kirwan (1975) and Okubo and Ebbesmeyer (1976). The estimated DKP variance decreases with increasing drifter number N. For three drifters, the LS technique yields an exact fit, hence for three drifters it is not possible to estimate DKP variance.

The LS technique of estimating DKPs was first applied to mesoscale flows, that is, $O(10)$ km length scales

Denotes content that is immediately available upon publication as open access.

Corresponding author: Matthew S. Spydell, mspydell@ucsd.edu

DOI: 10.1175/JTECH-D-19-0108.1

© 2019 American Meteorological Society. For information regarding reuse of this content and general copyright information, consult the AMS Copyright Policy (www.ametsoc.org/PUBSReuseLicenses).

Brought to you by IFREMER/BIBLIOTHEQUE LA | Unauthenticated | Downloaded 11/30/21 09:17 AM UTC

and ≥1 day time scales. For clusters of three drifters in the western Caribbean Sea (Molinari and Kirwan 1975), vorticity and divergence estimates were $O(10^{-1}f)$, where f is the local Coriolis parameter. Similar magnitudes of vorticity and divergence were found for mesoscale motions for clusters of five SOFAR floats (sampling at 300 m depth) deployed near the West Spitsbergen Current (Richez 1998). Improved GPS tracking technology has enabled DKP estimation for smaller space- and time-scale flows. For submesoscale eddies and fronts [$O(1)$ km length scales and $O(1)$ h time scales], vorticity and divergence estimates often exceed, and sometimes greatly (10 times), the local f based on clusters of nine GPS tracked near-surface drifters in the Santa Barbara channel (Ohlmann et al. 2017) and clusters of four drifters in the Gulf of Mexico (Ohlmann et al. 2019). Vorticity and divergence magnitudes decrease with increasing space and time scales (e.g., Ohlmann et al. 2017). Although calculating DKP at submesoscales and smaller is now possible, the role of errors in the LS technique at these scales is not completely understood.

The first study that applied the LS technique (Molinari and Kirwan 1975) noted very large "wiggles" in the DKP time series using clusters of three drifters. This is despite low-pass filtering the time series of positions (initial sampled at 15 min), from which the DKP was estimated, to approximately daily positions. These authors found that this error (i.e., wiggles) was inversely related to triangle (cluster) area. Vorticity estimated using clusters of five drifters near Point Reyes (California) was considered erroneous if the cluster area (each drifter is a polygon vertex), became too small ($<10^6\,\mathrm{m}^2$) or too large ($>4 \times 10^{10}\,\mathrm{m}^2$) (Paduan and Niiler 1990). For simulated drifters in a mesoscale model of the California Current System, noisy DKP rejection criteria used the longest drifter separation and the cluster ellipticity, defined as the ratio of the major to minor axis of the position covariance matrix (Righi and Strub 2001). The along cluster track Eulerian vorticity and drifter estimated vorticity were similar if the largest drifter separation was <20 km and if the cluster remained fairly circular. However, the grid resolution was approximately 9 km, hence, submesoscale dynamics were not properly resolved. A criterion based only on cluster ellipticity was used in Ohlmann et al. (2017).

DKP error depends on the velocity error, the number of drifters in the cluster, and the drifter cluster geometry (size and shape). Velocity error has two sources (Okubo and Ebbesmeyer 1976; Kirwan 1988): GPS instrument noise or processes noise by assuming spatially uniform velocity gradients in the Taylor series expansion. The velocity error has been a posteriori estimated from the LS misfit (Okubo and Ebbesmeyer 1976; Sanderson et al. 1988). Kirwan and Chang (1979) investigated the role of instrument noise on DKP error. However, explicit dependence of DKP error on cluster geometry was not determined and correlated velocity errors between instruments was not considered. Here, we focus only on the role of instrument noise on the velocity error.

Understanding GPS instrument error is critical as it contributes directly to DKP errors. On smaller scales, GPSs errors could be the main misfit contributor as the velocity Taylor series expansion (upon which the LS technique is based) is increasingly valid for decreasing spatial scales. However, GPS position and velocity errors can vary. For instance, GPS position errors sampling surfzone to shelf flows range from 1 to 10 m (Schmidt et al. 2003; Johnson and Pattiaratchi 2004; Ohlmann et al. 2005; Novelli et al. 2017). GPS position errors can be reduced to <0.01 m (Suara et al. 2015) using real-time kinematic (RTK) positioning. However, RTK systems are uncommon due to their cost, and are not appropriate for inner shelf to open-ocean studies due to needing a nearby base station. Although, GPS position error frequency spectra are red ($\approx f^{-2}$; Johnson and Pattiaratchi 2004; MacMahan et al. 2009; Suara et al. 2015), resulting in white (position differences) velocity error spectra. (MacMahan et al. 2009; Suara et al. 2015), the effect of filtering GPS positions and velocities on DKP errors is not completely understood.

In this article, GPS errors are investigated and quantified, and their effect on DKP, specifically vorticity, is examined. Although the errors associated with only one particular GPS receiver are investigated, the methodology here provides a template for use with any GPS. A simple illustrative formula for the vorticity error is derived and extended for clusters of N GPSs in section 2 and the appendix. In section 3, the GPSs, the observations, the data processing, and the statistical quantities of interest are described. In section 4, GPS position and velocity errors are presented and scalings for the vorticity error are tested. In the discussion (section 5), the vorticity error for in situ inner-shelf drifters is examined, previous DKP error analyses are contextualized, and the role of GPS satellite coverage investigated. The work is summarized is section 6.

2. Vorticity and vorticity errors from drifters

a. Vorticity error: An illustrative example

Consider velocity gradient error estimated from two still GPSs, one located at $X_1 = 0$, the other at $X_2 = L$. These GPSs measure positions $X_1 = x_1(t)$ and $X_2 = L + x_2(t)$ and Doppler velocities $u_1(t)$ and $u_2(t)$. This analysis is one dimensional for illustration and clarity. The time mean is indicated with an overbar thus, the mean of $x_1(t)$ is $\bar{x}_1$, hence, $x_1(t) = \bar{x}_1 + x_1'(t)$ where $\bar{x}_1$ is the mean error

Brought to you by IFREMER/BIBLIOTHEQUE LA | Unauthenticated | Downloaded 11/30/21 09:17 AM UTC

and $x_1'(t)$ the fluctuating error. For this analysis, we assume that x_1, x_2, u_1, and u_2 are correlated Gaussian random variables with nonzero mean and that the error statistics are identical for both GPSs. The position and velocity error variances are $\overline{(x_1')^2} = \overline{(x_2')^2} = \sigma_x^2$ and $\overline{(u_1')^2} = \overline{(u_2')^2} = \sigma_u^2$. The position and velocity error correlation on the same GPS is defined as $\overline{x_1'u_1'} = \sigma_x\sigma_u\rho_{x_1u_1}$, where ρ_{ab} represents correlation between random variables a and b. The position and velocity error correlation across GPSs is $\overline{x_1'u_2'} = \sigma_x\sigma_u\rho_{x_1u_2}$, and the velocity error correlation across different GPSs is $\overline{u_1'u_2'} = \sigma_u^2\rho_{u_1u_2}$.

The velocity gradient is estimated as a centered difference

$$\frac{dU(t)}{dX} = \frac{u_2(t) - u_1(t)}{L + x_2(t) - x_1(t)}. \tag{1}$$

Assuming that $L \gg |x_2 - x_1|$, the Taylor series expansion of (1) is

$$\frac{dU}{dx} = \frac{u_2 - u_1}{L}\left[1 - \frac{x_2 - x_1}{L} + \frac{(x_2 - x_1)^2}{L^2} - \ldots\right]. \tag{2}$$

To first order in $(x_2 - x_1)/L$, the mean velocity gradient is

$$\frac{d\overline{U}}{dx} = \frac{\overline{u}_2 - \overline{u}_1}{L} - \frac{1}{L^2}[-\overline{x_1u_1} + \overline{x_1u_2} + \overline{x_2u_1} - \overline{x_2u_2}], \tag{3}$$

where the first term on the right-hand side is zero if GPS velocities have no mean error. Because the statistics are the same for all GPSs, $\overline{x_1'u_2'} = \overline{x_2'u_1'}$ and $\overline{x_1'u_1'} = \overline{x_2'u_2'}$, we have

$$\frac{d\overline{U}}{dx} = \overbrace{\frac{(\overline{u}_2 - \overline{u}_1)}{L}\left[1 + \frac{(\overline{x}_1 - \overline{x}_2)}{L}\right]}^{\mathrm{I}} + \overbrace{\frac{2\sigma_x\sigma_u}{L^2}\left[\rho_{x_1u_2} - \rho_{x_1u_1}\right]}^{\mathrm{II}}. \tag{4}$$

Thus, velocity gradient mean error occurs if velocity mean error is nonzero (term I) or if velocity and position errors are correlated (term II), particularly if x' and u' are correlated differently on the same GPS than across GPSs. In practice, term II is much smaller than term I because for oceanographic scales of interest $\sigma_x \ll L$.

The mean square velocity gradient error is

$$\overline{\left(\frac{dU}{dx}\right)^2} = \overline{\left(\frac{u_2 - u_1}{L}\right)^2\left[1 - \frac{x_2 - x_1}{L} + \frac{(x_2 - x_1)^2}{L^2} - \ldots\right]^2} \tag{5}$$

or

$$\overline{\left(\frac{dU}{dx}\right)^2} = \overline{\left(\frac{u_1^2 + u_2^2 - 2u_1u_2}{L^2}\right)\left[1 - \frac{2(x_2 - x_1)}{L} + \frac{3(x_2 - x_1)^2}{L^2} + \ldots\right]}. \tag{6}$$

The expectation of the product of three zero-mean Gaussian random numbers is zero (the Isserlis theorem; Isserlis 1918), that is, $\overline{u_1'^2x_1'} = \overline{u_1'^2x_2'} = \overline{u_1'u_2'x_1'} = 0$, hence, the first two nonzero terms [in $(x_2 - x_1)/L$] are

$$\overline{\left(\frac{dU}{dx}\right)^2} = \frac{\overline{u_1^2 + u_2^2 - 2u_1u_2}}{L^2} + \frac{\overline{3(u_1^2 + u_2^2 - 2u_1u_2)(x_1^2 + x_2^2 - 2x_1x_2)}}{L^4}. \tag{7}$$

The first term dominates the velocity gradient mean square error; expanding it we have

$$\overline{\left(\frac{dU}{dx}\right)^2} = \frac{1}{L^2}(\overline{u}_1^2 + \overline{u}_2^2 - 2\overline{u}_1\overline{u}_2 + 2\sigma_u^2 - 2\overline{u_1'u_2'}), \tag{8}$$

such that the leading term of the squared velocity gradient standard error is

$$\sigma_{U_x}^2 \equiv \overline{\left(\frac{dU}{dx}\right)^2} - \left(\frac{d\overline{U}}{dx}\right)^2 = \frac{2\sigma_u^2}{L^2}\left(1 - \rho_{u_1u_2}\right). \tag{9}$$

Note that positive GPS to GPS velocity error correlations $\rho_{u_1u_2}$ decrease the velocity gradient standard error.

The vorticity $\zeta = dV/dx - dU/dy$ error is found from the gradient error. Assume that two drifters are aligned in the x direction and separated by L_x and two drifters aligned in y direction separated by L_y (a diamond pattern), assume $L_y \geq L_x$. For this configuration, the squared vorticity standard error is then

$$\sigma_\zeta^2 = \sigma_{V_x}^2 + \sigma_{U_y}^2. \tag{10}$$

Assuming u and v are independent with the same error statistics, we have $\sigma_{V_x}^2 = \sigma_{U_x}^2$, $\sigma_{U_y}^2 = \sigma_{V_y}^2$, and $\rho_{u_1u_2} = \rho_{v_1v_2}$, the squared vorticity standard error σ_ζ^2 is written as

$$\sigma_\zeta^2 = \frac{2\sigma_u^2}{L_x^2}\left(1 + \frac{L_x^2}{L_y^2}\right)\left(1 - \rho_{u_1u_2}\right). \tag{11}$$

Brought to you by IFREMER/BILIOTHEQUE LA | Unauthenticated | Downloaded 11/30/21 09:17 AM UTC

b. Estimating vorticity and vorticity errors from drifter cluster observations

Velocity gradients, and thus vorticity, can be estimated from $N \geq 3$ drifters (Molinari and Kirwan 1975) using a least squares method. Drifter velocities can be Taylor series expanded about the cluster center,

$$u_i = U + \frac{dU}{dx}x_i + \frac{dU}{dy}y_i + u_i', \qquad (12)$$

where U is the cluster mean velocity, dU/dx and dU/dy are velocity gradients over the cluster, and (x_i, y_i) are east–west (E-W) and north–south (N-S) positions relative to cluster center. The velocity residual u_i' is due to both instrument noise and process noise (the velocity field deviating from a spatially constant velocity gradient). With N drifter velocities and positions, the model parameters

$$\boldsymbol{\beta} = [U\, dU/dx\, dU/dy]^{\mathrm{T}} \qquad (13)$$

are found by least squares fit (minimizing mean square u') to the observed velocities,

$$\boldsymbol{\beta} = (\mathbf{R}^{\mathrm{T}}\mathbf{R})^{-1}\mathbf{R}^{\mathrm{T}}\tilde{\mathbf{U}}, \qquad (14)$$

where $\tilde{\mathbf{U}} = [u_1 u_2 \ldots u_N]^{\mathrm{T}}$ is the vector of observed drifter velocities and $\mathbf{R}$ is the $N \times 3$ matrix

$$\mathbf{R} = \begin{pmatrix} 1 & x_1 & y_1 \\ 1 & x_2 & y_2 \\ \vdots & \vdots & \vdots \\ 1 & x_N & y_N \end{pmatrix}. \qquad (15)$$

The alongshore cluster mean velocity V and velocity gradients, dV/dx, and dV/dy, are found similarly. The vorticity ζ is then $\zeta = dV/dx - dU/dy$.

For a cluster of N drifters, the vorticity error variance is derived in (A11) in the appendix and is given by

$$\sigma_\zeta^2 = \frac{1}{N}\frac{\sigma_u^2}{l_a^2}\left(1 + \frac{l_a^2}{l_b^2}\right)\left(1 - \rho_{u_1 u_2}\right), \qquad (16)$$

where l_a and l_b ($l_a \leq l_b$) are the minor and major axis lengths of the drifter cluster, that is, eigenvalues of the position covariance matrix $\mathbf{P}$ [see (A10)]. Moreover, l_a can be considered the width, or narrowness, of the cluster and l_b the length of the cluster. The velocity error σ_u^2 is due to both instrument and process error. Here we focus only on the effects of instrument error on DKP error.

The vorticity error variance assumes uncorrelated u', v', but correlated u' between GPSs [see (16)]. It is analogous to the two drifter illustrative example in (11), but accounts for the drifters number N and cluster size and shape through l_a and l_b. This expression (16) can be used a priori if the velocity error σ_u is known. Furthermore, (16) indicates that vorticity standard error decreases as $N^{-1/2}$, indicating that large numbers of drifters are required to reduce vorticity error substantially.

3. GPS instruments, observations, and methods

a. GPS instruments

Off-the-shelf, hand-held, "GT-31" GPSs (henceforth GPSs) manufactured by Locosys Technology Inc. are used here. These GPSs have been used in previous oceanographic studies (Herbers et al. 2012; McCarroll et al. 2014; Pearman et al. 2014; Fiorentino et al. 2014; Slivinski et al. 2017). These GPSs are useful for surface oceanographic drifter applications as they are waterproof to IPX7 standards and, due to their small size (9 cm × 5.8 cm × 2.5 cm), easily fit in a small otter box that can be mounted to various drifter bodies. These GPSs record position and Doppler shift (based on the frequency shift of the GPS carrier frequency) estimated velocity at 1 Hz using the SiRF Star 3 GPS chip. The 1 Hz sampling of these GPS is faster than required to sample submesoscale processes that evolve on tens of minutes to hourly time scales and faster than previous drifter studies of these motions (e.g., D'Asaro et al. 2018). However, as shorter time- and space-scale processes are investigated (e.g., Ohlmann et al. 2017), rapid sampling is needed for 1) understanding GPS errors dependence on sampling frequency, 2) surface wave spectra estimation as submesoscale processes may depend on Stokes drift (Hamlington et al. 2014), and 3) filtering out surface gravity waves. For example, nearshore vorticity can be $O(10^{-2})$ s^{-1} (Suanda and Feddersen 2015; Kumar and Feddersen 2017) not far from surface gravity wave frequencies (0.05 s^{-1}).

The SiRF chip GPS position–velocity solution algorithm is proprietary, and thus the relationship between position and Doppler velocity is unknown. The manufacturer states that horizontal positions have 10 m rms absolute accuracy and horizontal Doppler velocities have 0.1 m s^{-1} rms accuracy. Surface gravity wave spectra at $f > 0.05$ Hz have been accurately estimated from 1 Hz GT GPS horizontal positions (Herbers et al. 2012). These GPSs return a time series of (latitude, longitude) which is converted to distances using a WGS84 spheroid. The (easting, northing) component of 1 Hz raw position and velocity is $\mathbf{X}_r(t) = (X_r, Y_r)$ and $\mathbf{u}_r(t) = (u_r, v_r)$, respectively. These GPSs also record at 1 Hz the number of satellites in the GPS constellation

Brought to you by IFREMER/BIBLIOTHEQUE LA | Unauthenticated | Downloaded 11/30/21 09:17 AM UTC

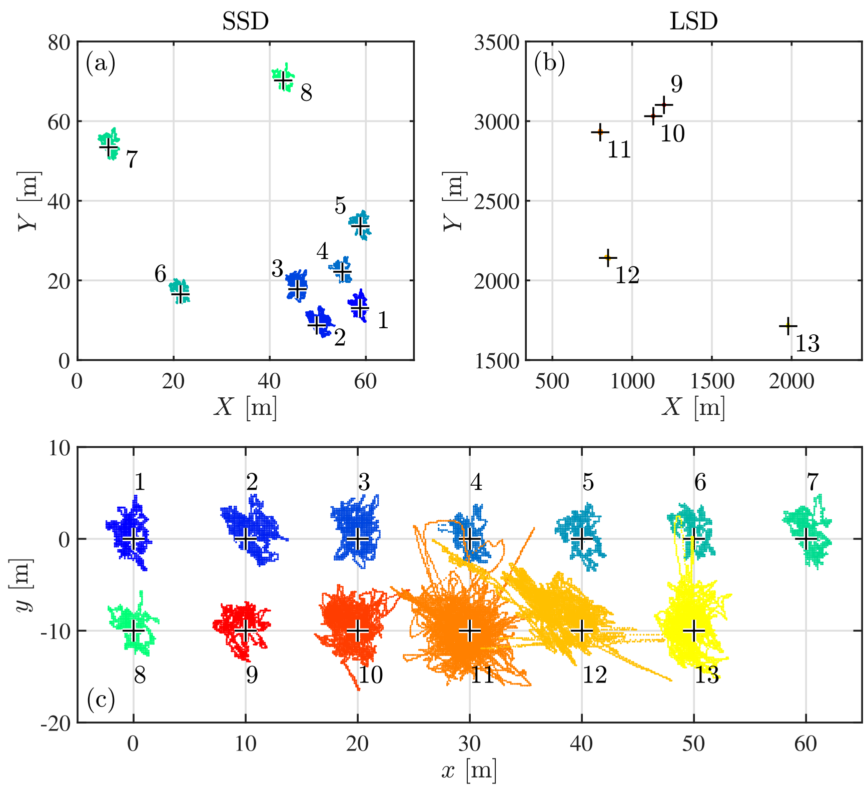

FIG. 1. Absolute GPS positions (X, Y) for the (a) small-scale stationary deployment (SSD) and (b) absolute GPS positions (X, Y) for the large-scale stationary deployment (LSD). In (b), colored positions are not visible because the scale of the position scatter is too small relative to the GPS separations. In (a) and (b), the deployed location is indicated by "+" and GPS reference numbers are indicated. (c) Relative positions (x, y), to the deployed location (+), for both deployments (with 10 m offsets). Note that colors will be consistent throughout Figs. 2, 4, and 5.

and a unitless estimate of the horizontal position error (HDOP).

b. Stationary deployments

There were two stationary deployments of multiple GPSs in Monterey, CA. For these stationary deployments, the "exact" position $\mathbf{X}_0$ of the GT was obtained by placing a survey grade RTK-GPS (≈1 cm accuracy; Suara et al. 2015) at the same location of the GT. Note that such stationary deployments can be used to quantify the error of any GPS. The deviation from the true position for each GPS is then $\mathbf{x}_r(t) = \mathbf{X}_r(t) - \mathbf{X}_0$, where $\mathbf{x}_r(t)$ is the "raw" 1 Hz position error time series (the subscript r denotes 1 Hz raw quantities).

For the first stationary deployment (30 July 2018), denoted the small-scale deployment (SSD), eight GPSs were placed in two squares for 18 h: a small square with 10 m sides (GPSs 1–4) and larger square with ≈40 m sides (GPSs 5–8, Fig. 1a). The SSD relative raw 1 Hz positions $\mathbf{x}_r(t)$ meander about ±2 m for each GPS (cool colors, Fig. 1b). For the second deployment (12 September 2018, duration of 24 h), denoted the large-scale deployment (LSD), the five GPS separations were larger, O(100–1000) m, than the SSD and GPS placement was not structured (cf. Figs. 1b,a). The LSD relative positions meandered between about ±2 m (GPS 9) to ±5 m (GPS 11) (warm colors, Fig. 1b).

For the SSD, the GPS satellite constellation changed little across GPSs, with 8.9 ± 1.2 satellites in view for each SSD GPS, where 8.9 is the mean (over the 8 GPSs) of the time-mean satellite number and 1.2 is the mean (over the 8 GPSs) of the time-standard deviation. The LSD deployment had slightly worse satellite coverage, with 8.6 ± 1.2 satellites in view (average over GPSs 9, 10, 11, and 13). GPS 12 had the worst satellite coverage, seeing 7.7 satellites in view on average. The GPS estimate of HDOP averaged 1.0 for all GPSs except GPS 12 where HDOP averaged 1.2 over the deployment. The HDOP standard deviation was approximately 0.2 for all GPSs except GPS 12 where it was 0.3.

Brought to you by IFREMER/BILIOTHEQUE LA | Unauthenticated | Downloaded 11/30/21 09:17 AM UTC

c. *In situ drifter observations*

In situ drifter observations from the ONR funded Inner Shelf Experiment conducted near Point Sal, California, during September–October 2017 are used here. Coastal Ocean Dynamics Experiment (CODE) surface drifter bodies (Davis 1985) equipped with 1 Hz Lycocos GT-31 GPSs were deployed for ≈5 h on multiple days on the inner shelf (5–40 m water depth). Drifters followed the mean horizontal flow between approximately 0.3 and 1.2 m below the surface. The water following properties of CODE drifters is well established (Poulain 1999; Novelli et al. 2017).

d. *Data processing*

The stationary and in situ processing steps are as follows. For the stationary deployments, GPSs had at most one missing velocity or position over the deployment duration (≈1 day) which was filled with linear interpolation. First, outlier Doppler velocities $|u_r(t)|$ greater than three standard deviations of u_r (but not positions) are removed and filled by linear interpolation. The fraction of outlier velocities was <0.08% for the SSD and between 0.013% and 0.50% for the LSD deployment. Second, velocities based on position differences, denoted $\dot{x}_r$, are obtained by centered difference, $\dot{x}_r(t) = [X_r(t+\delta t) - X_r(t-\delta t)]/(2\delta t)$. These velocities will be called position-derived velocities (PDVs). Thus, $\dot{x}_r(t)$ is the PDV error time series for the stationary deployments. Outliers are not removed for the PDV time series because doing so results in PDV time series equal to zero due to the discrete distribution of $\dot{x}$ (Figs. 2c,d).

Surface gravity wave motions do not contribute to submesoscale vertical vorticity but can contribute to noise in vorticity estimates. The surface gravity wave influence on raw velocities, positions, and PDVs are removed by low-pass filtering in the frequency domain with a Gaussian filter $G(f) = \exp[-(f/f_c)^2]$, where f_c is the low-pass-filter cutoff frequency. A variety of cutoff frequencies are considered, all at $f_c \le 4 \times 10^{-2}$ Hz below the sea-swell frequency band. If f_c is not specified, the default largest value $f_c = 4 \times 10^{-2}$ Hz is used. The resulting low-passed E-W time series are $u(t)$, $x(t)$, and $\dot{x}(t)$. To summarize, raw unfiltered quantities are denoted with a subscript r, low-passed quantities are not subscripted, and if not specified, the default value of $f_c = 4 \times 10^{-2}$ Hz is used.

e. *Stationary deployment error statistics and spectra*

The error statistics are now defined for the E-W components of position x and velocity u. For the jth GPS, the E-W mean position error is estimated as

$$\overline{x}_j = \frac{1}{N_j}\sum_{i=1}^{N_j} x_j(t_i), \tag{17}$$

where N_j is the number of 1 Hz samples. For the jth GPS, E-W position standard error $\sigma_{x,j}$ is estimated as

$$\sigma_{x,j} = \left[\frac{1}{N_j}\sum_{i=1}^{N_j} x_j(t_i)^2 - \overline{x}_j^2\right]^{1/2}. \tag{18}$$

Doppler and PDV velocity mean error ($\overline{u}$ and $\overline{\dot{x}}$, respectively) and standard error (σ_u and $\sigma_{\dot{x}}$, respectively) are defined similarly. The N-S components of these statistics are also defined similarly. The correlation between E-W velocity on GPS j and E-W velocity on GPS k is denoted $\rho_{u_j u_k}$ and estimated as

$$\rho_{u_j u_k} = \frac{1}{\sigma_{u,j}\sigma_{u,k}N_j}\sum_{i=1}^{N_j}[u_j(t_i) - \overline{u}_j][u_k(t_i) - \overline{u}_k]. \tag{19}$$

The correlation between E-W PDV on GPS j and GPS k ($\rho_{\dot{x}_j\dot{x}_k}$) is defined similarly as are the correlations for N-S velocities. This notation allows statistics to vary between GPSs that are separated by a distance l

$$l = \sqrt{(X_k - X_j)^2 + (Y_k - Y_j)^2}. \tag{20}$$

Note, the notation now uses the subscripts j and k, rather than 1 and 2 as in section 2a.

Error frequency spectra for each GPS is calculated from time series of raw GPS position errors $x_r(t)$, velocity error $u_r(t)$, and PDVs $\dot{x}_r(t)$, the respective error spectra are denoted $S_{xx}(f)$, $S_{uu}(f)$, and $S_{\dot{x}\dot{x}}(f)$. The spectra are estimated using a multitaper technique (e.g., Prieto et al. 2009) with 6 degrees of freedom (dof) and approximately 3×10^{-4} Hz frequency resolution. Means are removed from each time series prior to spectra calculation.

4. Results: Stationary deployments

a. *Time series*

GPS E-W relative position x, E-W PDV $\dot{x}$, and E-W Doppler velocity u, are shown in Fig. 2 (left column: SSD; right column: LSD) for the default low-pass-filter cutoff frequency $f_c = 4 \times 10^{-2}$ Hz. N-S position errors y, PDV $\dot{y}$, and velocity v are similar to the E-W errors and therefore not shown. E-W positions x meander about ±1.5 m for the SSD (Fig. 2a), the E-W PDV $\dot{x}$ fluctuates approximately ±0.025 m s^{-1} (Fig. 2c), and Doppler velocities u fluctuate approximately ±0.05 m s^{-1} (Fig. 2e). For the LSD, the position error time series x for GPS 9 (red) and GPS 13 (yellow), and PDVs, are similar to SSD GPSs (cf. Figs. 2a,b and 2c,d), whereas positions (especially at higher frequency) and PDVs for GPSs

Brought to you by IFREMER/BIBLIOTHEQUE LA | Unauthenticated | Downloaded 11/30/21 09:17 AM UTC

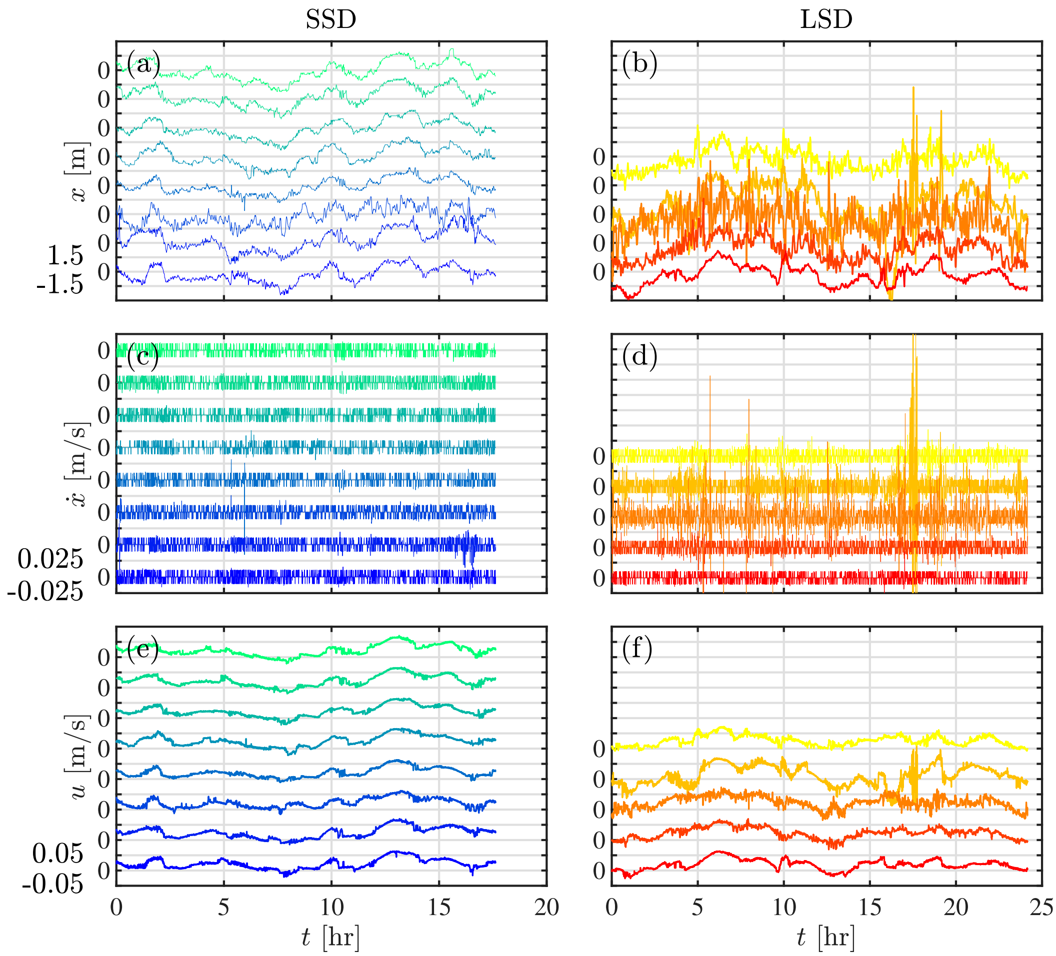

FIG. 2. Time series of (a),(b) E-W relative position (offset in y by 3 m), (c),(d) E-W PDV (offset in y by 0.05 m s^{-1}), and (e),(f) E-W velocity (offset in y by 0.1 m s^{-1}) for (a),(c),(e) small-scale and (b),(d),(f) large-scale stationary deployment.

10–12 are noisier. Velocity errors u for LSD GPSs are similar to the velocity error for SSD GPSs, although more higher-frequency error is evident for GPSs 10–12 (cf. Figs. 2e,f). Position x, and velocity u appear correlated from GPS to GPS (Figs. 2a,b,e,f).

Using the method described in section 2b, the time series of vorticity ζ (scaled by f at 35°) for the SSD and LSD, using GPSs 5, 6, and 7 and GPSs 9, 12, and 13, respectively, show the influence of GPS separation on vorticity error (Figs. 3a,b). For the small-scale deployment (GPSs separated ≈40 m), using $\dot{x}$ for the velocities in the best fitting method, that is, (12), results in a vorticity error time series fluctuating between approximately $\pm 5f$ (red curve, Fig. 3a) whereas for the LSD (GPSs separated ≈1000 m) the error time series is approximately $\pm 0.5f$ (red curve, Fig. 3b). We note, however, that this vorticity estimate is based on drifter separations smaller (40 and 1000 m), and containing higher-frequency PDVs (up to 25 s motions), than typical for submesoscale vorticity estimation that have separation scales of ≈2000 m and time-scales ≥600 s (e.g., Ohlmann et al. 2017). Using Doppler u for the velocities in (12) results in lower-frequency fluctuations with larger errors than using $\dot{x}$. For u, for the small-scale deployment $-5 < \zeta/f < 15$ and for the large-scale deployment $-1 < \zeta/f < 2$ (cf. red and black curves in Figs. 3a,b). The difference between vorticity estimated from u and PDV suggests that at lower frequency, vorticity from PDV is more accurate than u.

b. Error statistics on an individual GPS

The statistics of stationary GPS positions $x(t)$, velocities $u(t)$, and PDVs $\dot{x}(t)$ for the filter default low-pass-filter cutoff frequency ($f_c = 4 \times 10^{-2}$ Hz) time series are now presented. The E-W mean error $\overline{x}$ is negative for all GPSs except 2 and 7 (circles in Fig. 4a and Table 1) whereas $\overline{y}$ is positive for all GPSs (squares, Fig. 4a). The mean error $\overline{x}$ and $\overline{y}$ is <1 m, except for GPS 12 where

Brought to you by IFREMER/BIBLIOTHEQUE LA | Unauthenticated | Downloaded 11/30/21 09:17 AM UTC

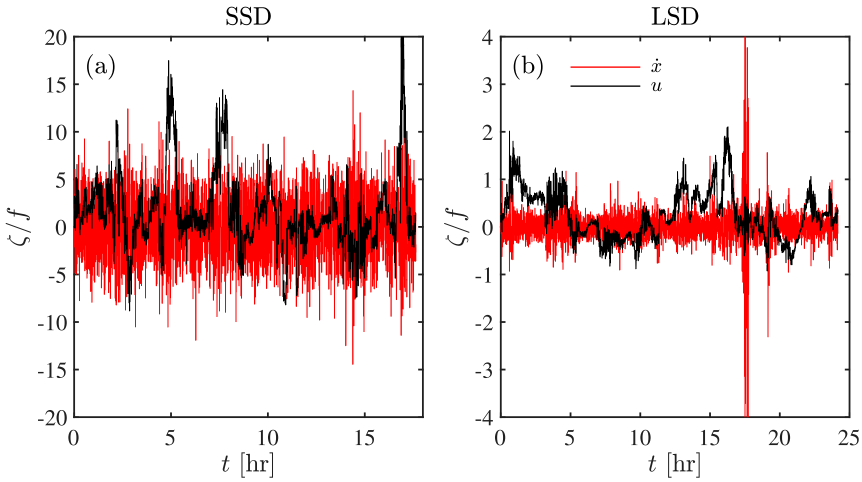

FIG. 3. (a) Stationary GPS vorticity (scaled by f at 35°) vs time for the small-scale deployment with separation of ≈40 m. Black line: using u_i from GPSs 5, 6, and 7; red line: using $\dot{x}_i$ from GPSs 5, 6, and 7. (b) Stationary GPS vorticity (scaled by f at 35°) vs time for the large-scale deployment with separations of ≈1000 m. Black line: using u_i from GPSs 9, 12, and 13; red line: using $\dot{x}_i$ from GPSs 9, 12, and 13.

$|\overline{x}|$ and $|\overline{y}| \approx 2.2$ m (Table 1). The E-W position standard error σ_x was approximately ≤1 m for the SSD (Fig. 4a, Table 1). E-W position standard errors for the LSD were generally larger than those for the SSD, although position standard errors for GPSs 9 and 13 were similar to SSD values (Table 1). The N-S position standard errors σ_y were larger in magnitude than σ_x with GPSs 10, 11, 12, and 13 having noticeably larger σ_y than the other GPSs (Table 1).

E-W velocity mean errors $\overline{u} \approx 0.025\,\mathrm{m\,s^{-1}}$ for both SSD and LSD, except GPS 12 which had smaller $\overline{u}$ (circles, Fig. 4c, Table 1). The N-S velocity mean error is negative with $|\overline{v}| \le 0.01\,\mathrm{m\,s^{-1}}$ for both deployments except GPS 12, where $\overline{v}$ is positive (squares, Fig. 4c, Table 1). E-W velocity standard errors σ_v are $\le 0.02\,\mathrm{m\,s^{-1}}$ except for GPS 12 where $\sigma_u = 0.032\,\mathrm{m\,s^{-1}}$ (bars, Fig. 4c, Table 1). N-S velocity standard errors σ_v are larger than σ_u by approximately 50%. The E-W and N-S PDV mean error $\overline{\dot{x}}$ and standard error $\sigma_{\dot{x}}$ are very small relative to the velocity mean and standard error (Fig. 4b). Moreover, the mean errors are $\overline{\dot{x}} \approx \overline{\dot{y}} \approx 0$ whereas the standard error $\sigma_{\dot{x}} \le 0.01\,\mathrm{m\,s^{-1}}$ except for GPSs 11 and 12. Thus, for velocities containing all frequencies up to $f = 4 \times 10^{-2}$ Hz, PDVs are more accurate than Doppler velocities.

c. GPS-to-GPS correlations

As outlined in section 2a, the velocity correlation from one GPS to another affects vorticity errors [see (11)]. GPS-to-GPS velocity–velocity correlations $\rho_{u_j u_k}$ are greater than 0.5 (Fig. 5a), whereas the PDV–PDV correlation $\rho_{\dot{x}_j \dot{x}_k}$ is much smaller (<0.1) (cf. Fig. 5a and Fig. 5b). Both the velocity–velocity and PDV–PDV correlations are smaller for the large-scale deployment (orange and red symbols, $l \ge 100$ m) than the small-scale deployment (blue symbols, $l < 100$ m) suggesting that correlations decrease with increasing GPS separation l. A correlation is red if it includes GPS 12 which had particularly poor satellite coverage relative to the other GPSs. Approximate 95% correlation significant levels are 0.6 for $\rho_{u_j u_k}$ and 0.03 for $\rho_{\dot{x}_j \dot{x}_k}$ (gray dashed lines, Fig. 5) with the number of independent data calculated using 83 min and 25 s (e-folding times) as decorrelation time scales (Thomson and Emery 2014). Hence, most $\rho_{u_j u_k}$ are significantly nonzero, except for the LSD $\rho_{u_j u_k}$ containing GPS 12. For PDVs, only some $\rho_{\dot{x}_j \dot{x}_k}$ for the SSD are significantly nonzero. Note that correlations that include GPS 12, the GPS with the largest errors and worst satellite coverage, are smaller (red symbols, Figs. 5a,b).

d. Error spectra

The spectra of raw positions S_{xx}, PDVs $S_{\dot{x}\dot{x}}$, and velocities S_{uu} are now presented (Fig. 6). The spectra of N-S and E-W position for each individual GPS is averaged (light colored thin lines in Fig. 6a) resulting in 12 dof for each spectra (thin lines). The N-S and E-W spectra are also averaged for PDV and velocity (light colored thin lines in Figs. 6b,c). The spectra for each GPS are averaged over the SSD and LSD (thick blue and red curves, respectively, Figs. 6a–c) resulting in 96 ($2 \times 6 \times 8$) dof for average SSD spectra and 60 ($2 \times 6 \times 5$) dof for average LSD spectra. Note that spectra are shown only for frequencies less than the default low-pass-filter cutoff frequency $f_c = 4 \times 10^{-2}$ Hz.

Brought to you by IFREMER/BILIOTHEQUE LA | Unauthenticated | Downloaded 11/30/21 09:17 AM UTC

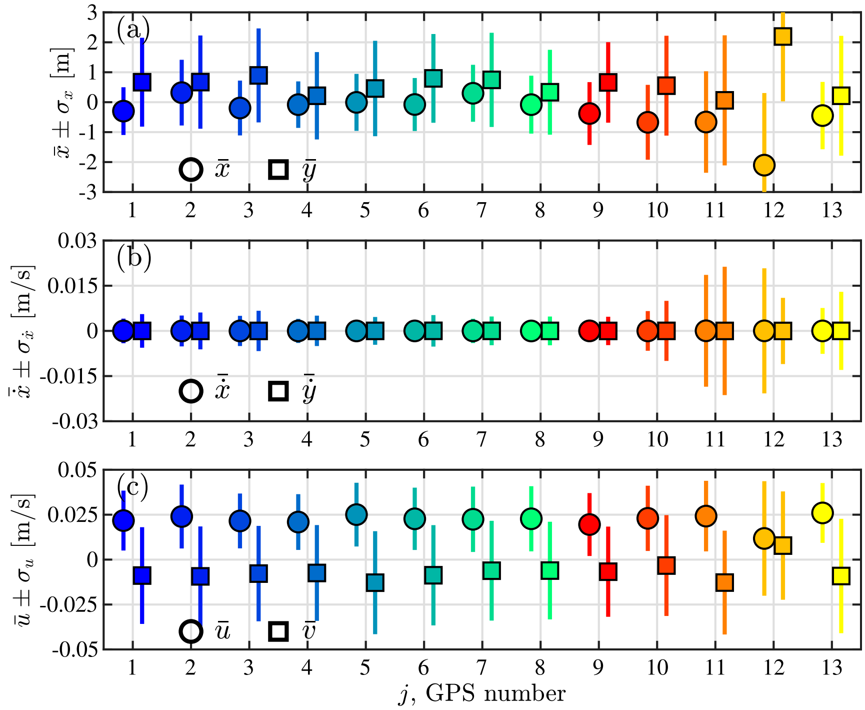

FIG. 4. (a) Position mean error $\bar{x}$ (circles) and $\bar{y}$ (squares) plus and minus position standard error σ_x vs GPS number. (b) Position differences $\bar{\dot{x}}$ (circles) and $\bar{\dot{y}}$ (squares) plus and minus position differences standard deviation $\sigma_{\dot{x}}$ vs GPS number. (c) Velocity mean error $\bar{u}$ (circles) and $\bar{v}$ (squares) plus and minus velocity standard error σ_u vs GPS number. GPSs 1–8 (cool colors) are from the small-scale stationary deployment, and GPSs 9–13 (warm colors) are from the large-scale stationary deployment.

For the small-scale deployment, the position error spectra $S_{xx}(f)$ follows an approximate f^{-2} scaling for $f > 10^{-4}$ Hz (cf. blue curve and dashed line, Fig. 6a). A similar spectral slope for GPS position errors has been previously reported (Johnson and Pattiaratchi 2004; MacMahan et al. 2009; Suara et al. 2015). The spectra $S_{xx}(f)$ flattens for $f \le 10^{-4}$ Hz because this is the approximate frequency resolution.

The velocity error spectra $S_{uu}(f)$ is also red but falls of more slowly, than the position error spectra $S_{xx}(f)$ (Fig. 6b). The SSD and LSD PDV error spectra is nearly white (blue and red curves, Fig. 6c) because the PDV is the time derivative of position. Comparing S_{uu} (reproduced in gray in Fig. 6c) and $S_{\dot{x}\dot{x}}(f)$ indicates that Doppler velocity u errors are smaller than PDV $\dot{x}$ errors for approximately $f > 10^{-3}$ Hz whereas for lower frequencies PDVs have smaller error than Doppler velocities.

TABLE 1. Statistics for the 13 stationary GPSs. GPSs 1–8 are from the SSD and GPSs 9–13 are from the LSD.

	1	2	3	4	5	6	7	8	9	10	11	12	13
$\bar{x}$ (cm)	−30	32	−19	−8	−1	−8	30	−8	−38	−67	−66	−210	−45
$\bar{y}$ (cm)	67	67	89	21	46	79	75	33	66	55	6	220	21
σ_x (cm)	80	110	92	78	95	88	95	97	105	125	169	241	112
σ_y (cm)	148	156	157	146	159	148	158	142	134	167	217	217	200
$\bar{u}$ (cm s^{-1})	2.2	2.4	2.2	2.1	2.5	2.3	2.2	2.3	2.0	2.3	2.4	1.2	2.6
$\bar{v}$ (cm s^{-1})	−0.9	−0.9	−0.8	−0.7	−1.3	−0.9	−0.6	−0.6	−0.3	−0.3	−1.3	0.8	−0.9
σ_u (cm s^{-1})	1.7	1.8	1.5	1.6	1.8	1.7	1.8	1.8	1.8	1.8	2.0	3.2	1.7
σ_v (cm s^{-1})	2.7	2.8	2.7	2.7	2.9	2.8	2.8	2.7	2.5	2.8	2.9	3.0	3.2
$\bar{\dot{x}}$ ($\times 10^{-3}$ cm s^{-1})	−1.6	−2.3	−1.3	−0.9	−0.9	−0.7	−0.8	−2.4	0.21	−0.7	3.3	1.7	−0.7
$\bar{\dot{y}}$ ($\times 10^{-3}$ cm s^{-1})	−0.4	−1.2	−0.9	1.7	0.3	2.0	0.9	−0.3	−1.4	0.3	−1.0	−2.1	0.4
$\sigma_{\dot{x}}$ (mm s^{-1})	4.1	5.1	5.0	4.0	3.5	3.6	4.0	3.6	3.7	6.6	18.6	20.8	7.6
$\sigma_{\dot{y}}$ (mm s^{-1})	5.6	6.1	6.7	5.0	4.6	5.2	4.8	4.8	4.7	10.0	21.3	11.0	13.0

Brought to you by IFREMER/BILIOTHEQUE LA | Unauthenticated | Downloaded 11/30/21 09:17 AM UTC

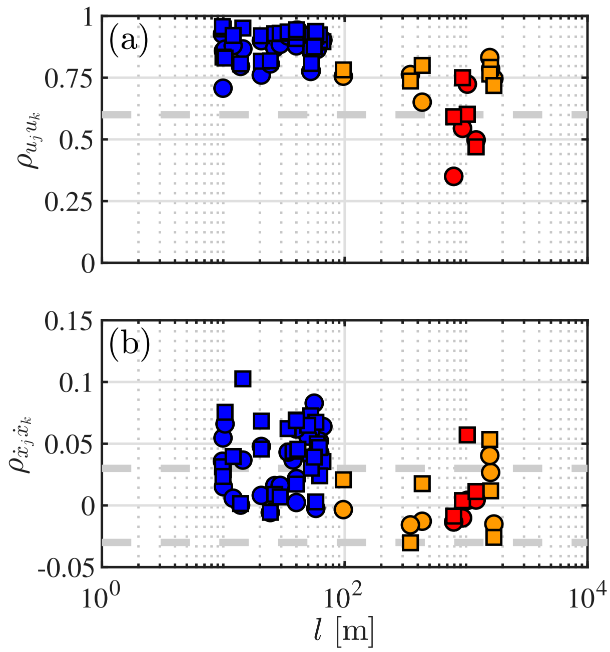

FIG. 5. GPS-to-GPS position correlations vs separation l. (a) Velocity–velocity correlations $\rho_{u_j u_k}$ and (b) PDV–PDV correlation $\rho_{\dot{x}_j \dot{x}_k}$. E-W correlations are circles and N-S correlations are squares. Small-scale deployments are blue and large-scale deployments are orange (or red if the correlation includes GPS 12). All correlations are calculated for raw time series filtered using the default low-pass-filter cutoff frequency $f_c = 4 \times 10^{-2}$ Hz. Approximate 95% nonzero correlation values are dashed gray lines.

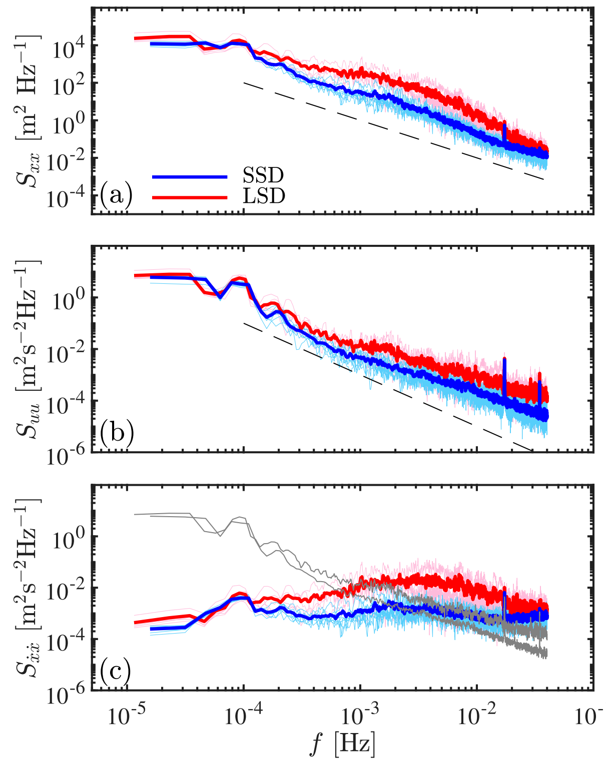

FIG. 6. (a) Position error spectra S_{xx}, (b) velocity error spectra S_{uu}, and (c) PDV error spectra $S_{\dot{x}\dot{x}}$ vs frequency f for the small-scale deployment (blue) and large-scale deployment (red). E-W and N-S components are averaged. Thin light-colored curves are from each GPS and the thick lines are the mean over the GPSs. In (a) and (b) f^{-2} is shown as the dashed black line. In (c), the gray lines are $S_{uu}(f)$ from (b) for reference.

e. Blended trajectory

The velocity S_{uu} and PDV spectra $S_{\dot{x}\dot{x}}$ indicate that for low frequencies ($f \lesssim 10^{-3}$ Hz), $\dot{x}$ velocities have less error than u velocities, whereas for higher frequencies ($f \gtrsim 10^{-3}$ Hz), u velocities have less error than $\dot{x}$ velocities. Thus, $S_{\dot{x}\dot{x}}(f) < S_{uu}(f)$ for $f < f_T$ whereas $S_{\dot{x}\dot{x}}(f) > S_{uu}(f)$ for $f > f_T$. The transition frequency is approximately $f_T \approx 10^{-3}$ Hz because $S_{\dot{x}\dot{x}}$ and S_{uu} cross at approximately this frequency (Fig. 6c). Note, that $\int_0^{4\times10^{-2}\mathrm{Hz}} S_{\dot{x}\dot{x}}(f')\,df' < \int_0^{4\times10^{-2}\mathrm{Hz}} S_{uu}(f')\,df'$ so that $\sigma_{\dot{x}} < \sigma_u$ (see Figs. 4b,c and Table 1). A reduced error velocity time series, however, would use $\dot{x}$ for the low frequency and u for the high frequency. This blended velocity u_B is then

$$u_B(t) = u(t) - \tilde{u}(t) + \widetilde{\dot{x}}(t), \tag{21}$$

where $\tilde{u}(t)$ and $\widetilde{\dot{x}}(t)$ are low passed at low-pass-filter cutoff frequency $f_c = 10^{-3}$ Hz. Recall that $u(t)$ is filtered at the default low-pass-filter cutoff frequency $f_c^{-1} = 25$ s, so that blended velocities contain motions with periods $\geq$25 s. For all 13 GPSs, blended raw velocity time series $u_B(t)$ are calculated. Note, that the blended time series are shorter than $u(t)$ and $\dot{x}(t)$ due to the low-pass filtering at $f_c = 10^{-3}$ Hz which necessitates removing some of the beginning and end of $u(t)$ and $\dot{x}(t)$. The difference in trajectory lengths results in small blended velocity and PDV spectra differences and small PDV–PDV correlation and blended velocity–velocity correlation differences for frequencies $< 10^{-3}$ Hz. These differences, however, are not statistically significant. Blended trajectories x_B,

$$x_B(t) = \int_0^t u_B(t')\,dt', \tag{22}$$

are also be constructed and follow the low-frequency drifter trajectory but have more accurate higher-frequency excursions. Blended trajectories are used for the in situ observations (section 5a). We note that typical studies of submesoscale motions (where the sampling $f < 10^{-3}$ Hz) do not require using blended velocities or trajectories because PDVs have smaller errors at these frequencies. However, blended velocities should be used, if possible, when sampling motions with time scales $>10^{-3}$ Hz.

Brought to you by IFREMER/BILIOTHEQUE LA | Unauthenticated | Downloaded 11/30/21 09:17 AM UTC

f. Dependence of velocity errors and correlation on the low-pass-filter cutoff frequency

The effect of the low-pass-filter cutoff frequency f_c on the velocity standard error and velocity–velocity correlation is now explored for SSD and LSD. The velocity standard error dependence on f_c [$\sigma_u(f_c)$] is calculated as the square root of the integral of the velocity error spectra (Fig. 6, thick curves)

$$\sigma_u(f_c) = \left[\int_0^{f_c} S_{uu}(f)\,df\right]^{1/2}. \qquad (23)$$

The f_c dependence of the PDV standard error $\sigma_{\dot{x}}(f_c)$ and blended velocity error $\sigma_{u_B}(f_c)$ are similarly estimated. Recall that spectra for the SSD and LSD are averaged over all GPSs in the deployment and across E-W and N-S components. Frequency-dependent velocity–velocity correlations are calculated using velocities filtered at various low-pass-filter cutoff frequencies $f_c > 2 \times 10^{-4}$ Hz. At lower frequencies, too few independent data exist for reliable correlations. Low-pass-filter cutoff-frequency–dependent SSD and LSD correlations are averaged over all GPS pairs (i.e., all j and k for $j \neq k$ in $\rho_{u_j x_k}$) and averaged over the E-W and N-S components.

The PDV error $\sigma_{\dot{x}}(f_c)$ monotonically increases with the low-pass-filter cutoff frequency f_c (see blue and red dotted curves in Fig. 7a). Because the PDV error spectra is approximately white, the error generally follows $\sigma_{\dot{x}}(f_c) \sim f_c^{1/2}$ for $f_c < 5 \times 10^{-3}$ Hz. For the lowest frequencies, the velocity error σ_u starts large, relative to $\sigma_{\dot{x}}$, but quickly asymptotically approaches a constant value (dashed curves in Fig. 7a) owing to the redness of $S_{uu}(f)$. Only near the highest frequency ($f_c = 4 \times 10^{-2}$ Hz), are the velocity error σ_u and the PDV error $\sigma_{\dot{x}}$ similar (cf. dashed and dotted curves in Fig. 7a). Due to their construction, blended velocity errors follow PDV errors for low frequencies and asymptotically approach a constant value for approximately $f_c > 10^{-3}$ Hz, less than either the u or $\dot{x}$ error. For $f_c < 10^{-3}$ Hz, σ_{u_B} is not statistically different from $\sigma_{\dot{x}}(f_c)$. Consistent with previous error statistics, the velocity standard error dependence on the low-pass-filter cutoff frequency f_c is larger for the LSD deployment than the SSD (red curves are above blue in Fig. 7a).

The velocity–velocity correlation $\rho_{u_j u_k}$ decreases with increasing low-pass-filter cutoff frequency f_c for u, $\dot{x}$, and u_B (dashed curves, Fig. 7b). For u, $\rho_{u_j u_k}(f_c)$ starts large ($\geq$0.7) and decreases by about 0.1 with increasing f_c. Both $\rho_{\dot{x}\dot{x}}$ and $\rho_{u_B u_B}$, are relatively large for $f_c < 10^{-3}$ Hz and decreases quickly with values <0.1 for larger f_c (dotted and solid curves, Fig. 7b). Like the standard error, blended velocity correlation is not statistically different from the PDV correlation for $f_c < 10^{-3}$ Hz. SSD (blue curves Fig. 7b) velocity, PDV, and blended velocity GPS-to-GPS correlations are greater than their corresponding LSD correlations (red curves Fig. 7b) consistent with the individual GPS-to-GPS correlations in Fig. 5.

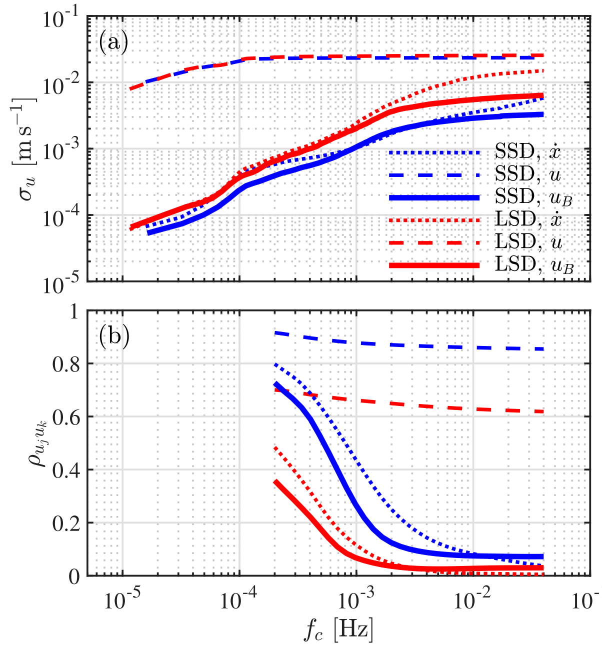

FIG. 7. The frequency dependence of quantities related to vorticity standard error. Small-scale (SSD) and large-scale (LSD) deployments are blue and red curves, respectively. (a) Velocity error σ_u and (b) the velocity–velocity correlation between different GPSs $\rho_{u_j u_k}$ ($j \neq k$) vs low-pass-filter cutoff frequency f_c. Statistics for $\dot{x}$ are dotted, u are dashed, and blended velocity u_B are solid. Correlations for $f < 2 \times 10^{-4}$ are not shown because there are not enough independent samples for these frequencies.

g. Scaling the vorticity error

Here, scalings for the mean vorticity and vorticity error for the stationary GPSs are tested. The effect of the velocity type (u, $\dot{x}$, or u_B), the effect of low-pass-filter cutoff frequency f_c, and the effect of the minor axis length l_a are examined. Clusters of three drifters are defined from triplets of SSD and LSD GPSs. The SSD has eight clusters (Fig. 1a) made of GPS numbers (1, 2, 3), (2, 3, 4), (3, 4, 1), (4, 1, 2), (5, 6, 7), (6, 7, 8), (7, 8, 5), and (8, 5, 6). From the eigenvalues of the cluster position covariance matrix, clusters 1–4 have minor and major axes of $l_a \approx 4$ m and $l_b \approx 7$ m and clusters 5–8 have $l_a \approx 16$ m and $l_b \approx 7$ m. The LSD has three clusters (Fig. 1b) made up of GPS numbers (9, 11, 12), (9, 12, 13) and (10, 12, 13). For the first cluster, $(l_a, l_b) = (180, 530)$ m and for the remaining clusters $(l_a, l_b) \approx (430, 800)$ m. For each cluster and velocity type, least squares vorticity is

Brought to you by IFREMER/BIBLIOTHEQUE LA | Unauthenticated | Downloaded 11/30/21 09:17 AM UTC

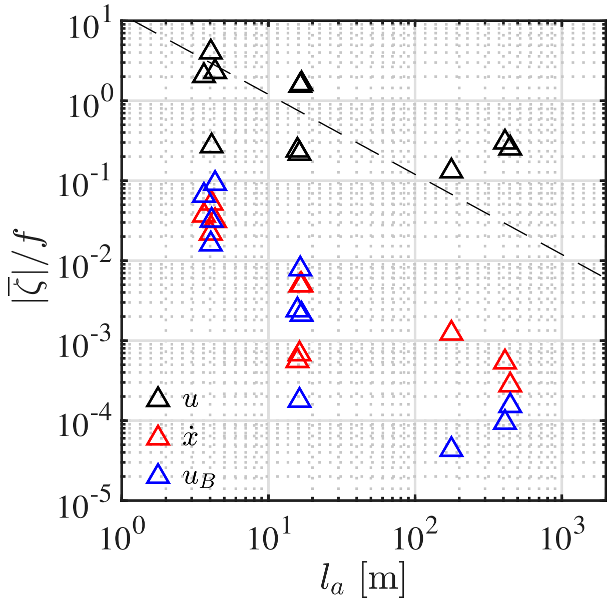

FIG. 8. Absolute value of the mean vorticity (scaled by f at 35°) for clusters of three stationary GPSs (triangles) vs the minor axis length l_a of the GPS cluster. Small- and large-scale deployments are separated by $l_a = 100$ m. Vorticity derived from Doppler velocities u are black, PDVs $\dot{x}$ are red, and blended velocities u_B are blue. All velocities are filtered at the low-pass-filter cutoff frequency $f_c = 4 \times 10^{-2}$ Hz. The dashed line is $\propto l_a^{-1}$. There is no frequency dependence since the standard deviations are of the mean velocity, which does not change with f_c. Blue and red triangles are not exactly the same since the length of the time series are different due to the low passing required in the construction of u_B.

calculated for three different low-pass-filter cutoff frequencies $f_c^{-1} = (25,\ 300,\ 1800)$ s resulting in 99 (11 clusters of three GPSs, 3 velocity products, and 3 f_c) vorticity time series from which (as GPSs are stationary) vorticity mean error $\bar{\zeta}$ and standard error σ_ζ are calculated. Additionally, σ_ζ is estimated a priori from (16) using σ_u (and $\sigma_{\dot{x}}$, σ_{u_B}) and $\rho_{u_j u_k}$ (and $\rho_{\dot{x}_j \dot{x}_k}$, $\rho_{u_{Bj} u_{Bk}}$) associated with the appropriate f_c (Fig. 7) and respective SSD or LSD l_a (Table 1). Recall that velocity variances and correlations are averages of E-W and N-S values.

The vorticity mean error magnitude $|\bar{\zeta}|/f$ is inversely related to the cluster minor axis l_a (dashed line, Fig. 8). For the Doppler velocities u, $|\bar{\zeta}|/f > 0.1$ regardless of minor axis l_a (black triangles, Fig. 8), whereas for $\dot{x}$ and u_B, $|\bar{\zeta}|/f < 0.1f$ (red and blue triangles, Fig. 8), as the $\bar{\dot{x}}$ and $\bar{u}_B$ are much smaller than $\bar{u}$ (Fig. 4). Note that $|\bar{\zeta}|/f$ is independent of the low-pass-filter cutoff frequency f_c because it derives from the time mean of the velocity.

For all low-pass-filter cutoff frequencies f_c and all velocity products, the vorticity standard error σ_ζ/f decreases as l_a^{-1} from l_a of 5–400 m (Fig. 9). For the highest $f_c^{-1} = 25$ s, the vorticity standard error σ_ζ/f varies from

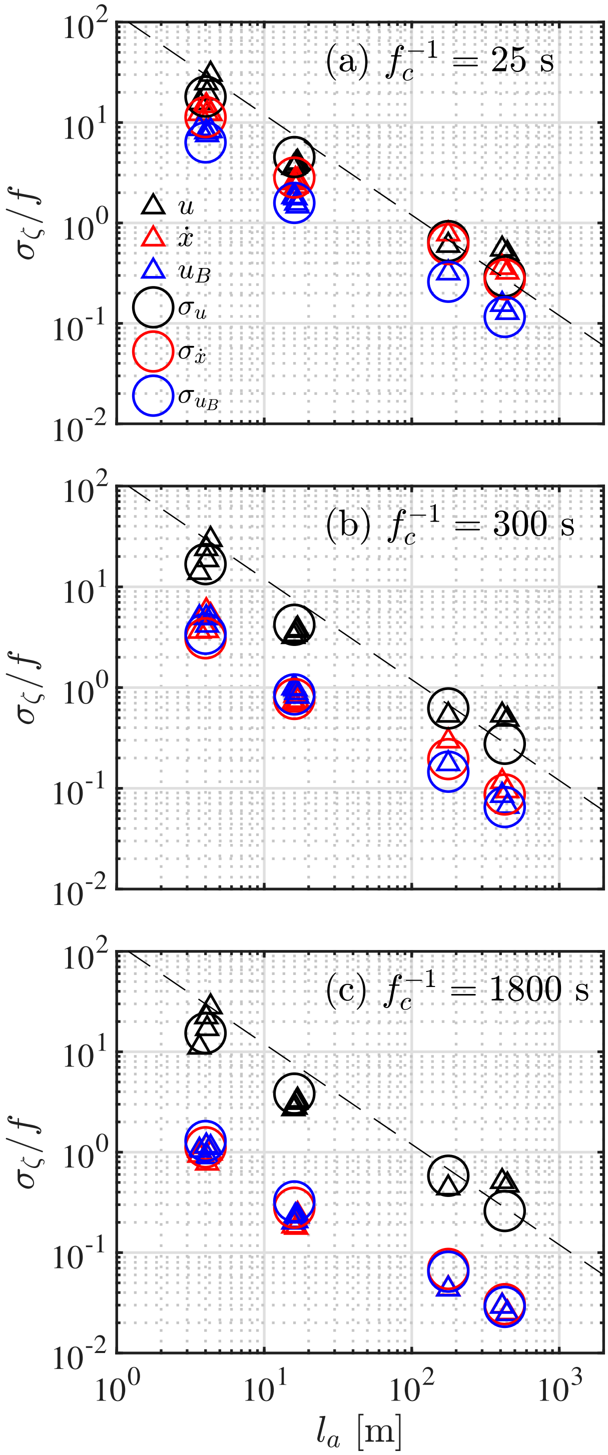

FIG. 9. Vorticity standard error for clusters of three stationary GPSs for the small- and large-scale stationary deployment. Standard deviation of cluster vorticity (triangles, scaled by f at 35°) vs l_a for velocities filtered at (a) $f_c^{-1} = 25$ s, (b) $f_c^{-1} = 300$ s, and (c) $f_c^{-1} = 1800$ s. The small- and large-scale deployments are separated by $l_a = 100$ m. Vorticity is derived from velocities u (black), PDVs $\dot{x}$ (red), or blended velocities u_B (blue). Dashed black lines in all panels are $\propto l_a^{-1}$. Large circles are found using (16): values of each term are listed in Table 2.

Brought to you by IFREMER/BIBLIOTHEQUE LA | Unauthenticated | Downloaded 11/30/21 09:17 AM UTC

TABLE 2. Terms used to evaluate the vorticity standard error σ_ζ, (16), for the SSD ($l_a = 4$ and 16 m) and LSD ($l_a = 177$ and 427 m) drifter clusters in Fig. 9. Velocity standard errors (columns 3–5) and correlations (columns 6–8) are low-pass frequency cutoff dependent (column 9).

l_a (m)	l_b (m)	σ_u (m s^{-1})	$\sigma_{\dot{x}}$ (m s^{-1})	σ_{u_B} (m s^{-1})	$\rho_{u_j u_k}$	$\rho_{\dot{x}_j \dot{x}_k}$	$\rho_{u_{Bj} u_{Bk}}$	f_c^{-1} (s)
		0.0235	0.0058	0.0033	0.85	0.04	0.07	25
4	7	0.0234	0.0017	0.0018	0.87	0.17	0.09	300
		0.0232	0.0009	0.0009	0.89	0.61	0.48	1800
		0.0235	0.0058	0.0033	0.85	0.04	0.07	25
16	28	0.0234	0.0017	0.0018	0.87	0.17	0.09	300
		0.0232	0.0009	0.0009	0.89	0.61	0.48	1800
		0.0256	0.0150	0.0064	0.61	0.01	0.03	25
177	527	0.0251	0.0048	0.0036	0.64	0.03	0.03	300
		0.0246	0.0019	0.0017	0.67	0.23	0.15	1800
		0.0256	0.0150	0.0064	0.61	0.01	0.03	25
427	798	0.0251	0.0048	0.0036	0.64	0.03	0.03	300
		0.0246	0.0019	0.0017	0.67	0.23	0.15	1800

30 to 0.2 over the $l_a = 5$ m to $l_a = 400$ m and the different velocity products (Fig. 9a). The σ_ζ/f is 2–4 times larger using u relative to u_B, with $\dot{x}$ in between (cf. colored triangles in Fig. 9a). Using the Doppler velocity u, σ_ζ/f does not decrease substantially with decreasing f_c (cf. black triangles across Fig. 9), as much of the u error is at low frequencies and filtering has little effect (Figs. 6 and 7). In contrast, for the $\dot{x}$ and u_B, σ_ζ/f decreases an order of magnitude from $f_c^{-1} = 25$ s to $f_c^{-1} = 1800$ s at all l_a, consistent with the reduced error (Fig. 7). At $f_c^{-1} = 25$ s and $f_c^{-1} = 300$ s, the u_B-based σ_ζ/f is smallest as it combines the optimal frequency-dependent noise properties of u and $\dot{x}$ (Fig. 7). At $f_c^{-1} = 1800$ s, u_B and $\dot{x}$ σ_ζ/f are nearly identical. The small difference is because the time series u_B is shorter than $\dot{x}$.

For each velocity product, the vorticity standard error σ_ζ/f dependence on the length scales l_a and l_b is well reproduced by the error scaling (16) with $N = 3$ (cf. circles and triangles in Fig. 9). The small differences between stationary GPS σ_ζ/f and (16) are due to using SSD or LSD values of σ_u and $\rho_{u_j u_k}$ in (16) and not specific values for the GPS triplet. In contrast to previous, a posteriori error analysis (e.g., Okubo and Ebbesmeyer 1976), the similarity between the stationary GPS σ_ζ/f and the scaling (16) indicates that vorticity errors can be anticipated a priori with knowledge of the velocity error (and potential correlation) and the scale of drifter cluster. This will be useful in drifter experiment planning where vorticity and divergence are being estimated. Note that vorticity errors for drifters instrumented with other GPSs may differ due to different GPS instrument noise σ_u. However, the methods outlined here (sections 4b, 4c, 4d, and 4f) can be applied to any GPS in order to accurately estimate σ_u and therefore σ_ζ.

5. Discussion

a. Vorticity error for in situ data

The scaling (16) is now used to assess the influence of GPS error for in situ derived vorticity. Surface drifters were deployed in clusters on 10 October 2016 near Point Sal, California (34.9°N, −120.67°E). Here, an example of three clusters of three drifters over 5 h reveals a complex surface flow (Fig. 10). The two northern clusters (red and blue in Fig. 10) initially heads offshore, before advecting onshore and northward about 2 km.

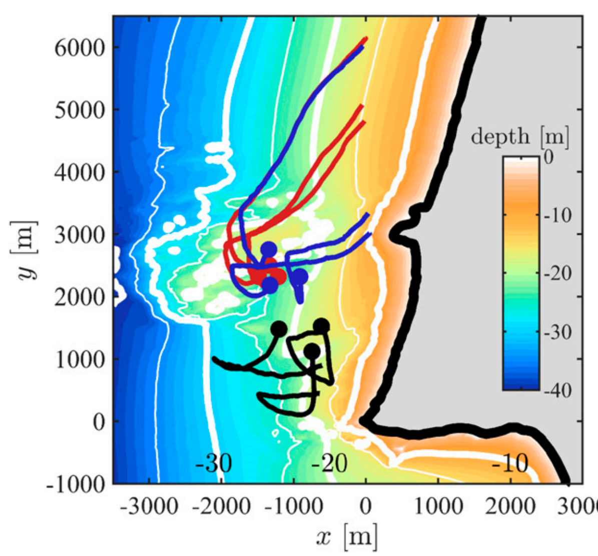

FIG. 10. Tracks of three clusters of three drifters for the 10 October drifter release (colored curves). Initial positions are indicated by dots. Bathymetry is contoured and thick white contours are at 10 m intervals while thin white contours are at 5 m intervals. N-S (y) and E-W (x) distances are relative to the tip of Point Sal, CA (34.9°N, −120.67°E).

Brought to you by IFREMER/BIBLIOTHEQUE LA | Unauthenticated | Downloaded 11/30/21 09:17 AM UTC

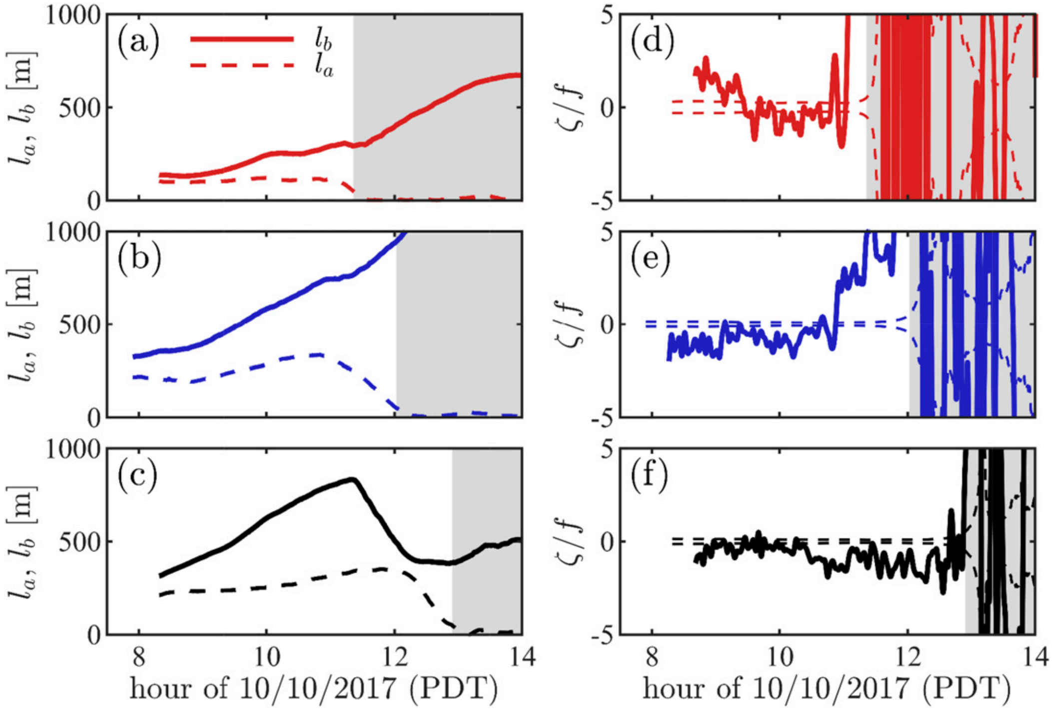

FIG. 11. (a)–(c) The minor l_a (dashed curves) and major l_a (solid curves) axis lengths vs time for the (top to bottom) red, blue, and black drifter clusters in Fig. 10. (d)–(f) The LS vorticity normalized by the local f (ζ/f) vs time for the three clusters. Vorticity is calculated using a 5-min low-pass frequency cutoff ($f_c^{-1} = 300$ s) blended velocities. In (d)–(f), thin dashed curves are plus and minus the vorticity standard error σ_ζ/f calculated using (16). Gray shading in all panels indicates times for which $l_a < 50$ m, corresponding to the time when σ_ζ/f increases rapidly.

In contrast, the southernmost cluster (black in Fig. 10) has weak advection. For all clusters, drifters are entrained in a frontal feature and end up aligned alongfront. The frontal nature of this feature was identified by temperatures recorded by nearby moorings: the surface temperature increased by ≈1°C from the shoreward to seaward side of the front (not shown).

For these three clusters and 5 h deployment, the minor l_a and major l_b axis lengths (Figs. 11a–c) are calculated from the drifter-position covariance matrix P, (A10), using blended positions x_B, (22), at every time step. The LS vorticity is estimated with the blended positions x_B and blended velocities u_B. Blended velocities u_B use a low-pass cutoff frequency of $f_c^{-1} = 300$ s. For each cluster, vorticity standard error σ_ζ is estimated using the scaling (16) with parameters $N = 3$, (l_a, l_b), the LSD derived $\sigma_{u_B} = 0.0036\,\mathrm{m\,s^{-1}}$, and with $\rho_{u_{Bj}u_{Bk}} = 0$. Note, assuming $\rho_{u_{Bj}u_{Bk}} = 0$ is a worst-case assumption and makes this error estimate an upper bound. The σ_ζ time dependence is due only to the changing cluster geometry (l_a, l_b).

For all clusters except the southern most (black), the cluster major axis $l_b(t)$ grows with time (solid curves, Figs. 11a–c). For all clusters, the minor axis $l_a(t)$ is at first largely constant (between 100 and 300 m depending on cluster) before decreasing rapidly at approximately 1100, 1100, and 1200 Pacific daylight time (PDT) for the red, blue, and black clusters, respectively (dashed curves, Figs. 11a–c). This rapid decrease is due to drifters being entrained into the frontal feature (Fig. 10). Times of frontal entrainment, that is, when $l_a < 50$ m, are shaded gray in Fig. 11. This alongfront drifter alignment with very small l_a/l_b ratio is typical of for surface drifter clusters in submesoscale features (Ohlmann et al. 2017). Prior to frontal entrainment, LS vorticity for each cluster is generally between $\pm 2f$ and can change by f on 1 h time scales with additional higher-frequency (0.3–0.5 h time scales) variability (Figs. 11d–f). During this time, the a priori vorticity standard error σ_ζ/f is relatively small, nearly always smaller than the σ_ζ/f (dashed curves in Fig. 11). The σ_ζ/f is largest for cluster "red" due to the smaller l_a and l_b (top panels of Fig. 11). Some of the higher-frequency σ_ζ/f variability in Figs. 10d–f is attributable to error as this variability has approximate amplitude of σ_ζ/f. Coincident with the l_a rapid decrease, σ_ζ/f begins oscillating widely beyond $\pm 5f$ at very high frequencies at approximately 1130, 1200, and 1300 PDT for the red, blue, and black cluster, respectively.

Brought to you by IFREMER/BILIOTHEQUE LA | Unauthenticated | Downloaded 11/30/21 09:17 AM UTC

This suggests that the vorticity is dominated by noise. Commensurate with these oscillations, the vorticity standard error σ_ζ/f increases rapidly precisely when l_a becomes very small (<50 m, shaded gray in Fig. 11). Hence, even for velocity errors of $\sigma_u \approx 0.004\,\mathrm{m\,s^{-1}}$, vorticity cannot be accurately estimated on scales of $l_a <$ 50 m with $N = 3$ m if that vorticity is $O(f)$.

b. Previous vorticity estimates and errors

Large errors in estimated DKP (i.e., vorticity, divergence) were previously evident (e.g., Molinari and Kirwan 1975; Paduan and Niiler 1990; Ohlmann et al. 2017) and a method to estimate DKP standard errors had been developed (Okubo and Ebbesmeyer 1976; Kirwan and Chang 1979) establishing the role of the velocity misfit σ_u, due to instrument error and process noise by assuming uniform velocity gradients. However, σ_u had to be estimated a posteriori from the LS fit, with some fraction of contribution from instrument noise. The relative contribution of instrument and process noise to σ_u will depend on the flow scales, drifter cluster size, and instrument noise. Here, the instrument velocity error σ_u and GPS-to-GPS error correlations ρ_{u_j,u_k} are estimated a priori for different low-pass-filter cutoff frequencies f_c. From this, DKP errors such as vorticity standard error σ_ζ can be known a priori rather a posteriori estimated. This method, (16), can be used to guide drifter experiment planning for accurately estimating vorticity and divergence.

The previous DKP error estimation method, (A4), embedded cluster geometry within $(\mathbf{R}^\mathrm{T}\mathbf{R})^{-1}$, and thus did not explicitly reveal the importance of the geometry. Because the precise role of cluster geometry on the errors was unknown, various ad hoc methods for determining when the DKP error was too large were developed. Previous authors have used area, effectively $l_a l_b$, (Paduan and Niiler 1990), ellipticity l_a/l_b (Ohlmann et al. 2017), or a combination of maximum drifter separation and ellipticity (Righi and Strub 2001), to determine when DKP errors become too large. Here, the precise role of the drifter cluster minor l_a and major l_b axes were established and

$$\sigma_\zeta^2 = N^{-1}\sigma_u^2 l_a^{-2}[1 + (l_a/l_b)^2]\left(1 - \rho_{u_j u_k}\right).$$

Thus, for highly elliptic clusters ($l_a \ll l_b$), the vorticity error is largely due to l_a, while for more circular clusters ($l_a \approx l_b$), the squared error depends on both l_a and l_b and for $l_b \approx l_a$ the squared error is ≈2 times the squared error for highly elliptic clusters. As such, large vorticity errors should be identified by $l_a^{-2} + l_b^{-2}$, rather than the area or ellipticity.

For the Point Sal estimated vorticity, comparing our direct predictions of the vorticity error (dashed lines in Figs. 11d–f) to the previous criterion is instructive. Recall that the time dependence of these errors arise only from the changing geometry of the drifter cluster, that is, $l_a(t)$ and $l_b(t)$, and that large vorticity errors resulted from $l_a < 50$ m. Previous authors suggested that vorticity errors depend on cluster area (Molinari and Kirwan 1975; Paduan and Niiler 1990) setting lower and upper limits to the area of the drifter cluster beyond which DKP errors are too large. Setting an upper limit is appropriate for large drifter separations where the process noise becomes large as the Taylor series approximation of the velocity, (12), from which the LS technique is built on, is no longer valid. A minimum ellipticity l_a/l_b criterion for detecting DKP noise has also been suggested (Ohlmann et al. 2017). Both a minimum area criterion and a minimum ellipticity criterion could be applied to the Point Sal clusters because for these clusters, area and ellipticity criterion are similar to the minimum l_a criterion (<50 m) used here. The time dependence of l_a and l_b in Figs. 11a–c indicate that until approximately 1100 PDT $l_a(t)$ remains fairly constant whereas $l_b(t)$ increases. For times greater than 1100, 1100, and 1200 PDT (red, blue, and black clusters, respectively), however, l_a rapidly decreases whereas l_b is relatively constant. Thus, the time dependence of l_a, $l_a l_b$, and l_a/l_b are all similar when $l_a(t)$ is rapidly decreasing. However, cluster minimum area or ellipticity criteria to distinguish high DKP noise will not in general give accurate results due to direct dependence of the vorticity standard error, (16), on l_a.

c. Effect of satellite coverage on errors

To get the most accurate estimate of vorticity errors from GPS tracked drifters, the underlying GPS velocity error must be known. In addition to depending on the particular GPS receiver, this error will depend on the quality of the GPS satellite constellation. The quality of the constellation depends on the number of satellites n_s in view and the position of these satellites in the sky. Although satellite position is not recorded by the GPSs used here, n_s and a nondimensional estimate of the absolute position error (HDOP), are recorded by these GPSs at 1 Hz. Because n_s only varied by 1.5 satellites over the SSD and LSD, effect of satellite number on GPS velocity errors cannot be thoroughly examined. Here, we briefly explore how satellite coverage affects GPS position and velocity standard errors for the stationary GPS dataset.

For this dataset, increasing satellite number $\overline{n}_s$ decreases the position standard error σ_x (Fig. 12a). Overall, LSD had smaller $\overline{n}_s$ (red dots, especially GPS 12) and larger σ_x than the SSD (blue dots). The PDV standard error $\sigma_{\dot{x}}$ and Doppler velocity standard error σ_u are similarly related to satellite number $\overline{n}_s$ (Figs. 12b,c). The GPS estimate of horizontal position error HDOP

Brought to you by IFREMER/BIBLIOTHEQUE LA | Unauthenticated | Downloaded 11/30/21 09:17 AM UTC

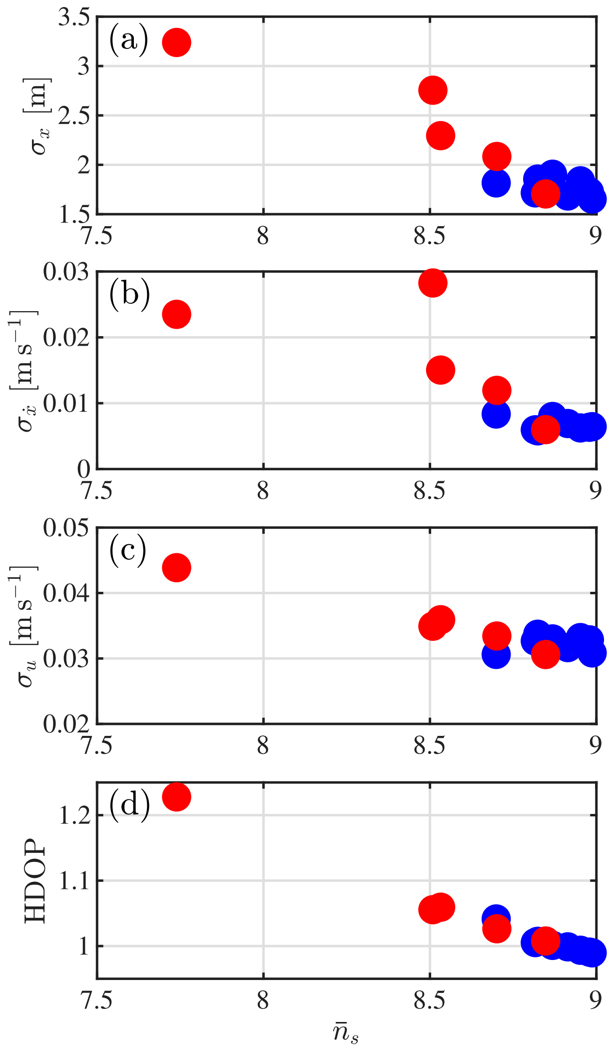

FIG. 12. (a) Position standard error σ_x, (b) PDV standard error $\sigma_{\dot{x}}$, (c) Doppler velocity standard error σ_u, and (d) HDOP vs the mean number of satellites in view $\overline{n}_s$. Colors refer to SSD (blue) and LSD (red). The standard errors are the square root of averaged E-W and N-S squared standard errors in Table 1. Values are found using the time series filtered at the default low-pass-filter frequency $f_c = 4 \times 10^{-2}$ Hz.

decreases approximately linearly with $\overline{n}_s$ (Fig. 12d), hence, HDOP provides a useful measure of position error. The relationship between error and $\overline{n}_s$ indicates that more precise estimates of GPS velocity errors are possible given satellite coverage information. This could be useful in order to distinguish signal and noise for vorticity estimates where the noise and signal magnitudes are similar, that is, for vorticity estimates at smaller space and time scales.

6. Summary

The a priori vorticity standard error σ_ζ is derived (16) based on the least squares method of estimating vorticity from drifters. The σ_ζ depends upon the velocity error (from instrument noise or process noise due to assuming uniform velocity gradients), cross-drifter correlation, drifter number, and drifter cluster shape. This derivation extended previous vorticity standard error estimates by including the effect of the correlated velocity errors and showing how the drifter cluster minor and major axes l_a, l_b affect the error.

Two stationary GPS experiments, with identically zero vorticity, were performed at separations of 10–700 m to understand drifter derived vorticity error and test the derivation using 1 Hz position differences (PDV) and Doppler shift velocities. Standard vorticity estimation reveals error of $\pm 5f$ at separations of 40 m. For low frequencies ($<10^{-3}$ Hz), PDVs velocities are more accurate than Doppler velocities, whereas at higher frequencies ($>10^{-3}$ Hz), the opposite occurs. A "blended" velocity is derived which has the low-frequency characteristics of PDV and the higher-frequency characteristics of the Doppler velocities, resulting in the smallest velocity error. The frequency-dependent velocity variances and GPS-to-GPS correlations were quantified as a function of low-pass-filter cutoff frequency. For the two stationary GPS experiments, the vorticity standard error as a function of cluster minor axis l_a is well predicted given velocity error and GPS-to-GPS correlation.

Vorticity error analysis is applied to three clusters of three GPS drifters released on the inner shelf off of Point Sal, California, that sampled submesoscale flow features. The value σ_ζ due to GPS noise was estimated a priori using (16). For these clusters, the vorticity was $O(f)$ but began to oscillate widely as the drifters were entrained in a frontal feature. The a priori estimated σ_ζ increases dramatically coincident with the large vorticity oscillations. This σ_ζ increases is due to small l_a (<50 m), and the drifter cluster minor axis (narrowness) is the key time-dependent factor affecting vorticity error. Even for velocity errors of 0.004 m s^{-1}, the vorticity error exceeds $\pm 5f$ when cluster minor axis <50 m. Large vorticity standard error cannot be anticipated based on cluster area ($l_a l_b$) or ellipticity (l_a/l_b). This a priori method for estimating vorticity standard error can be used in planning submesoscale drifter deployments where vorticity or divergence are being estimated.

Acknowledgments. The Office of Naval Research supported this research through grants N00014-5-1-2631 (SIO) and N0001418WX00229 (NPS). Casey Gon assisted in the stationary field deployments. For the Point Sal fieldwork, Bill Boyd, Greg Boyd, Tucker Freismuth, Casey Gon, Matt Gough, Rob Grenzeback, Derek Grimes, Ami Hansen, Paul Jessen, Michael Kovatch, Paul Lenz, Aaron Morrone, Andy O'Neill, Lucian Parry, Brett Pickering,

Brought to you by IFREMER/BIBLIOTHEQUE LA | Unauthenticated | Downloaded 11/30/21 09:17 AM UTC

Greg Sinnett, Kent Smith, Marla Stone, Ata Suanda, Brian Woodward, and Keith Wyckoff are acknowledged for their help in deployment and recovery. The authors thank Derek Grimes, Michael Kovatch, Jen Mackinnon, Sean Celona, Andre Paloczy, Nirnimesh Kumar, Ata Suanda, and Amy Waterhouse for providing useful feedback. The data and files necessary to reproduce the results herein, can be obtained by contacting the corresponding author (mspydell@ucsd.edu). We thank two reviewers for helping to improve the manuscript.

APPENDIX

Derivation of Vorticity Error Variance

Here, the vorticity standard error σ_ζ is derived explicitly including both cluster geometry (size and shape), and velocity correlations across drifters, extending previous work (Okubo and Ebbesmeyer 1976). For N drifters, the least squares inversion for $\boldsymbol{\beta} = [U\ dU/dx\ dU/dy]^{\mathrm{T}}$, (13), is given in (14) and the position matrix $\mathbf{R}$ is given in (15). The covariance of least squares fit model parameters β is given by (e.g., Wunsch 1996)

$$\mathrm{cov}(\boldsymbol{\beta}) = (\mathbf{R}^{\mathrm{T}}\mathbf{R})^{-1}\mathbf{R}^{\mathrm{T}}\tilde{\mathbf{U}}\tilde{\mathbf{U}}^{\mathrm{T}}\mathbf{R}(\mathbf{R}^{\mathrm{T}}\mathbf{R})^{-1}. \quad \text{(A1)}$$

Because positions (x_i and y_i) are relative to the cluster center, $\langle x\rangle = 0$ and $\langle y\rangle = 0$, where $\langle\cdot\rangle$ represent an average over all drifters. Thus, the matrix $\mathbf{R}^{\mathrm{T}}\mathbf{R}$ takes the form

$$\mathbf{R}^{\mathrm{T}}\mathbf{R} = N\begin{pmatrix} 1 & 0 & 0 \\ 0 & s_{xx}^2 & s_{xy}^2 \\ 0 & s_{xy}^2 & s_y^2 \end{pmatrix}, \quad \text{(A2)}$$

where the position covariances are defined as $s_{ab}^2 = \langle ab\rangle$, again averaged over all drifters. The $(\mathbf{R}^{\mathrm{T}}\mathbf{R})^{-1}$ matrix is given by

$$(\mathbf{R}^{\mathrm{T}}\mathbf{R})^{-1} = \frac{1}{N(s_{xx}^2 s_{yy}^2 - s_{xy}^4)}\begin{pmatrix} s_{xx}^2 s_{yy}^2 - s_{xy}^4 & 0 & 0 \\ 0 & s_{yy}^2 & -s_{xy}^2 \\ 0 & -s_{xy}^2 & s_{xx}^2 \end{pmatrix}. \quad \text{(A3)}$$

The velocity error covariance is $\tilde{\mathbf{U}}\tilde{\mathbf{U}}^{\mathrm{T}}$. Previously the velocity error covariance matrix was assumed diagonal (e.g., Okubo and Ebbesmeyer 1976), that is, errors are uncorrelated and homogeneous, and the covariance of the LS fit parameters is given by

$$\mathrm{cov}(\boldsymbol{\beta}) = \sigma_u^2(\mathbf{R}^{\mathrm{T}}\mathbf{R})^{-1} \quad \text{for} \quad \tilde{\mathbf{U}}\tilde{\mathbf{U}}^{\mathrm{T}} = \sigma_u^2\mathbf{I}, \quad \text{(A4)}$$

where $\mathbf{I}$ is the identity matrix and σ_u is the velocity error due to both instrument noise and process error (incorrectly assuming that velocity gradients are constant). Here, however, the velocities errors are assumed to be equally correlated across all GPSs with coefficient $\rho_{u_j u_k}$, thus

$$\begin{aligned}\tilde{\mathbf{U}}\tilde{\mathbf{U}}^{\mathrm{T}} &= \sigma_u^2\begin{pmatrix} 1 & \rho_{u_j u_k} & \rho_{u_j u_k} & \cdots \\ \rho_{u_j u_k} & 1 & \rho_{u_j u_k} & \cdots \\ \vdots & \vdots & \vdots & \ddots \end{pmatrix} \\ &= \underbrace{\sigma_u^2\rho_{u_j u_k}\begin{pmatrix} 1 & 1 & 1 & \cdots \\ 1 & 1 & 1 & \cdots \\ \vdots & \vdots & \vdots & \ddots \end{pmatrix}}_{\mathrm{A}} + \underbrace{\sigma_u^2\left(1-\rho_{u_j u_k}\right)\mathbf{I}}_{\mathrm{B}}. \end{aligned} \quad \text{(A5)}$$

Correlations of velocity error are approximately constant if drifter separations do not vary much, for example, correlations for the small- and large-scale (if GPS 12 is omitted) GPS deployments are approximately constant for each deployment (see Fig. 5a). The variance of the estimated mean velocity U, that is, $\mathrm{cov}(\boldsymbol{\beta})_{1,1}$, is

$$\sigma_U^2 = \rho_{u_j u_k}\sigma_u^2 + \frac{1}{N}\left(1-\rho_{u_j u_k}\right)\sigma_u^2, \quad \text{(A6)}$$

where the first term is from term A and the second from term B in (A5). The (3, 3) term of (A1) is the variance of the velocity gradient $\sigma_{dU/dy}^2$, and it is $\sigma_u^2(1-\rho_{u_j u_k})a_{33}$ where a_{33} is the (3, 3) term of (A3), thus,

$$\sigma_{dU/dy}^2 = \frac{\sigma_u^2}{N}\left(1-\rho_{u_j u_k}\right)\frac{s_{xx}^2}{s_{xx}^2 s_{yy}^2 - s_{xy}^4}. \quad \text{(A7)}$$

The vorticity error variance is

$$\sigma_\zeta^2 = \sigma_{dV/dx}^2 + \sigma_{dU/dy}^2 \quad \text{(A8)}$$

and if the E-W and N-S velocity errors are the same ($\sigma_v^2 = \sigma_u^2$), and assuming u and v errors are uncorrelated, the squared vorticity standard error is

$$\sigma_\zeta^2 = \frac{\sigma_u^2}{N}\left(1-\rho_{u_j u_k}\right)\frac{s_{xx}^2 + s_{yy}^2}{s_{xx}^2 s_{yy}^2 - s_{xy}^4}. \quad \text{(A9)}$$

If these assumptions are relaxed, a less elegant expression results.

The position covariances s_{xx}^2, s_{yy}^2, and s_{xy}^2 can be expressed as the eigenvalues l_a^2 and l_b^2 ($l_a \le l_b$) of the position covariance matrix $\mathbf{P}$:

$$\mathbf{P} = \begin{pmatrix} s_{xx}^2 & s_{xy}^2 \\ s_{xy}^2 & s_{yy}^2 \end{pmatrix} \quad \text{(A10)}$$

Brought to you by IFREMER/BIBLIOTHEQUE LA | Unauthenticated | Downloaded 11/30/21 09:17 AM UTC

in such a way that the vorticity error, (A9), in terms of l_a and l_b is

$$\sigma_\zeta^2 = \frac{\sigma_u^2}{N}(1-\rho_{uu})\left(\frac{1}{l_a^2}+\frac{1}{l_b^2}\right) \quad \text{(A11)}$$

which is (16). The eigenvalues l_a and l_b can be considered the width and length of the drifter cluster. This concise formula for the vorticity error variance differs from previous analysis (e.g., Okubo and Ebbesmeyer 1976; Kirwan and Chang 1979) in that explicitly accounts for the cluster geometry and accounts for potentially correlated velocity errors.

REFERENCES

Brown, J., J. MacMahan, A. Reniers, and E. Thornton, 2009: Surf zone diffusivity on a rip-channeled beach. *J. Geophys. Res.*, **114**, C11015, https://doi.org/10.1029/2008JC005158.

D'Asaro, E. A., and Coauthors, 2018: Ocean convergence and the dispersion of flotsam. *Proc. Natl. Acad. Sci. USA*, **115**, 1162–1167, https://doi.org/10.1073/pnas.1718453115.

Davis, R. E., 1985: Drifter observations of coastal surface currents during CODE: The method and descriptive view. *J. Geophys. Res.*, **90**, 4741–4755, https://doi.org/10.1029/JC090iC03p04741.

Fiorentino, L., M. Olascoaga, and A. Reniers, 2014: Analysis of water quality and circulation of four recreational Miami beaches through the use of Lagrangian Coherent Structures. *Mar. Pollut. Bull.*, **83**, 181–189, https://doi.org/10.1016/j.marpolbul.2014.03.054.

Hamlington, P. E., L. P. Van Roekel, B. Fox-Kemper, K. Julien, and G. P. Chini, 2014: Langmuir–submesoscale interactions: Descriptive analysis of multiscale frontal spindown simulations. *J. Phys. Oceanogr.*, **44**, 2249–2272, https://doi.org/10.1175/JPO-D-13-0139.1.

Herbers, T. H. C., P. F. Jessen, T. T. Janssen, D. B. Colbert, and J. H. MacMahan, 2012: Observing ocean surface waves with GPS-tracked buoys. *J. Atmos. Oceanic Technol.*, **29**, 944–959, https://doi.org/10.1175/JTECH-D-11-00128.1.

Isserlis, L., 1918: On a formula for the product-moment coefficient of any order of a normal frequency distribution in any number of variables. *Biometrika*, **12**, 134–139, https://doi.org/10.1093/biomet/12.1-2.134.

Johnson, D., and C. Pattiaratchi, 2004: Application, modelling and validation of surfzone drifters. *Coast. Eng.*, **51**, 455–471, https://doi.org/10.1016/j.coastaleng.2004.05.005.

Kirwan, A. D., 1988: Notes on the cluster method for interpreting relative motions. *J. Geophys. Res.*, **93**, 9337–9339, https://doi.org/10.1029/JC093iC08p09337.

——, and M.-S. Chang, 1979: Effect of sampling rate and random position error on analysis of drifter data. *J. Phys. Oceanogr.*, **9**, 382–387, https://doi.org/10.1175/1520-0485(1979)009<0382:EOSRAR>2.0.CO;2.

Kumar, N., and F. Feddersen, 2017: A new offshore transport mechanism for shoreline-released tracer induced by transient rip currents and stratification. *Geophys. Res. Lett.*, **44**, 2843–2851, https://doi.org/10.1002/2017GL072611.

LaCasce, J., 2008: Statistics from Lagrangian observations. *Prog. Oceanogr.*, **77**, 1–29, https://doi.org/10.1016/j.pocean.2008.02.002.

Lumpkin, R., and G. C. Johnson, 2013: Global ocean surface velocities from drifters: Mean, variance, El Niño–Southern Oscillation response, and seasonal cycle. *J. Geophys. Res. Oceans*, **118**, 2992–3006, https://doi.org/10.1002/jgrc.20210.

——, T. Özgökmen, and L. Centurioni, 2017: Advances in the application of surface drifters. *Annu. Rev. Mar. Sci.*, **9**, 59–81, https://doi.org/10.1146/annurev-marine-010816-060641.

MacMahan, J., J. Brown, and E. Thornton, 2009: Low-cost handheld Global Positioning System for measuring surf-zone currents. *J. Coastal Res.*, **253**, 744–754, https://doi.org/10.2112/08-1000.1.

McCarroll, R. J., R. W. Brander, I. L. Turner, H. E. Power, and T. R. Mortlock, 2014: Lagrangian observations of circulation on an embayed beach with headland rip currents. *Mar. Geol.*, **355**, 173–188, https://doi.org/10.1016/j.margeo.2014.05.020.

Molinari, R., and A. D. Kirwan, 1975: Calculations of differential kinematic properties from Lagrangian observations in the western Caribbean Sea. *J. Phys. Oceanogr.*, **5**, 483–491, https://doi.org/10.1175/1520-0485(1975)005<0483:CODKPF>2.0.CO;2.

Novelli, G., C. M. Guigand, C. Cousin, E. H. Ryan, N. J. M. Laxague, H. Dai, B. K. Haus, and T. M. Özgökmen, 2017: A biodegradable surface drifter for ocean sampling on a massive scale. *J. Atmos. Oceanic Technol.*, **34**, 2509–2532, https://doi.org/10.1175/JTECH-D-17-0055.1.

Ohlmann, J. C., P. F. White, A. L. Sybrandy, and P. P. Niiler, 2005: GPS-cellular drifter technology for coastal ocean observing systems. *J. Atmos. Oceanic Technol.*, **22**, 1381–1388, https://doi.org/10.1175/JTECH1786.1.

——, M. J. Molemaker, B. Baschek, B. Holt, G. Marmorino, and G. Smith, 2017: Drifter observations of submesoscale flow kinematics in the coastal ocean. *Geophys. Res. Lett.*, **44**, 330–337, https://doi.org/10.1002/2016GL071537.

——, L. Romero, E. Pallas-Sanz, and P. Perez-Brunius, 2019: Anisotropy in coastal ocean relative dispersion observations. *Geophys. Res. Lett.*, **46**, 879–888, https://doi.org/10.1029/2018GL081186.

Okubo, A., and C. C. Ebbesmeyer, 1976: Determination of vorticity, divergence, and deformation rates from analysis of drogue observations. *Deep-Sea Res.*, **23**, 349–352, https://doi.org/10.1016/0011-7471(76)90875-5.

Ollitrault, M., and A. Colin de Verdière, 2014: The ocean general circulation near 1000-m depth. *J. Phys. Oceanogr.*, **44**, 384–409, https://doi.org/10.1175/JPO-D-13-030.1.

Paduan, J. D., and P. P. Niiler, 1990: A Lagrangian description of motion in Northern California coastal transition filaments. *J. Geophys. Res.*, **95**, 18 095–18 109, https://doi.org/10.1029/JC095iC10p18095.

Pearman, D., T. Herbers, T. Janssen, H. van Ettinger, S. McIntyre, and P. Jessen, 2014: Drifter observations of the effects of shoals and tidal-currents on wave evolution in San Francisco Bight. *Cont. Shelf Res.*, **91**, 109–119, https://doi.org/10.1016/j.csr.2014.08.011.

Poulain, P.-M., 1999: Drifter observations of surface circulation in the Adriatic Sea between December 1994 and March 1996. *J. Mar. Syst.*, **20**, 231–253, https://doi.org/10.1016/S0924-7963(98)00084-0.

Prieto, G., R. Parker, and F. L. Vernon III, 2009: A Fortran 90 library for multitaper spectrum analysis. *Comput. Geosci.*, **35**, 1701–1710, https://doi.org/10.1016/j.cageo.2008.06.007.

Richez, C., 1998: The West Spitsbergen Current as seen by SOFAR floats during the ARCTEMIZ 88 experiment: Statistics, differential kinematic properties, and potential vorticity balance. *J. Geophys. Res.*, **103**, 15 539–15 565, https://doi.org/10.1029/97JC02421.

Righi, D. D., and P. Strub, 2001: The use of simulated drifters to estimate vorticity. *J. Mar. Syst.*, **29**, 125–140, https://doi.org/10.1016/S0924-7963(01)00013-6.

Brought to you by IFREMER/BIBLIOTHEQUE LA | Unauthenticated | Downloaded 11/30/21 09:17 AM UTC

Sanderson, B. G., B. K. Pal, and A. Goulding, 1988: Calculations of unbiased estimates of the magnitude of residual velocities from a small number of drogue trajectories. *J. Geophys. Res.*, **93**, 8161–8162, https://doi.org/10.1029/JC093iC07p08161.

Schmidt, W. E., B. T. Woodward, K. S. Millikan, R. T. Guza, B. Raubenheimer, and S. Elgar, 2003: A GPS-tracked surf zone drifter. *J. Atmos. Oceanic Technol.*, **20**, 1069–1075, https://doi.org/10.1175/1460.1.

Slivinski, L., L. Pratt, I. Rypina, M. Orescanin, B. Raubenheimer, J. MacMahan, and S. Elgar, 2017: Assimilating Lagrangian data for parameter estimation in a multiple-inlet system. *Ocean Modell.*, **113**, 131–144, https://doi.org/10.1016/j.ocemod.2017.04.001.

Spydell, M. S., F. Feddersen, R. T. Guza, and W. E. Schmidt, 2007: Observing surf-zone dispersion with drifters. *J. Phys. Oceanogr.*, **37**, 2920–2939, https://doi.org/10.1175/2007JPO3580.1.

Suanda, S. H., and F. Feddersen, 2015: A self-similar scaling for cross-shelf exchange driven by transient rip currents. *Geophys. Res. Lett.*, **42**, 5427–5434, https://doi.org/10.1002/2015GL063944.

Suara, K., C. Wang, Y. Feng, R. J. Brown, H. Chanson, and M. Borgas, 2015: High-resolution GNSS-tracked drifter for studying surface dispersion in shallow water. *J. Atmos. Oceanic Technol.*, **32**, 579–590, https://doi.org/10.1175/JTECH-D-14-00127.1.

Thomson, R. E., and W. J. Emery, 2014: *Data Analysis Methods in Physical Oceanography*. 3rd ed. Elsevier, 728 pp.

Wunsch, C., 1996: *The Ocean Circulation Inverse Problem*. Cambridge University Press, 458 pp., https://doi.org/10.1017/CBO9780511629570.

Brought to you by IFREMER/BILIOTHEQUE LA | Unauthenticated | Downloaded 11/30/21 09:17 AM UTC